Velocity-scalar filtered mass density function for large eddy simulation of turbulent reacting flows

M. R. H. Sheikhi[a] and P. Givi
Department of Mechanical Engineering and Materials Science, University of Pittsburgh, Pittsburgh, Pennsylvania 15261, USA

S. B. Pope
Sibley School of Mechanical and Aerospace Engineering, Cornell University, Ithaca, New York 14853, USA

(Received 29 November 2006; accepted 11 July 2007; published online 26 September 2007)

A methodology termed the "velocity-scalar filtered mass density function" (VSFMDF) is developed and implemented for large eddy simulation (LES) of variable-density turbulent reacting flows. This methodology is based on the extension of the previously developed "velocity-scalar filtered density function" method for constant-density flows. In the VSFMDF, the effects of the unresolved subgrid scales (SGS) are taken into account by considering the joint probability density function of the velocity and scalar fields. An exact transport equation is derived for the VSFMDF in which the effects of SGS convection and chemical reaction are in closed forms. The unclosed terms in this equation are modeled in a fashion similar to that in Reynolds-averaged simulation procedures. A set of stochastic differential equations (SDEs) are considered which yield statistically equivalent results to the modeled VSFMDF transport equation. The SDEs are solved numerically by a Lagrangian Monte Carlo procedure in which the Itô-Gikhman character of the SDEs is preserved. The consistency of the proposed SDEs and the convergence of the Monte Carlo solution are assessed. In nonreacting flows, it is shown that the VSFMDF results agree well with those obtained by a "conventional" finite-difference LES procedure in which the transport equations corresponding to the filtered quantities are solved directly. The VSFMDF results are also compared with those obtained by the Smagorinsky closure, and all the results are assessed via comparison with data obtained by direct numerical simulation of a temporally developing mixing layer involving transport of a passive scalar. It is shown that all of the first two moments including the scalar fluxes are predicted well by the VSFMDF. Moreover, the VSFMDF methodology is shown to be able to represent the variable density effects very well. The predictive capabilities of the VSFMDF in reacting flows are further demonstrated by LES of a reacting shear flow. The predictions show favorable agreement with laboratory data, and demonstrate several of the features as observed experimentally. © *2007 American Institute of Physics*. [DOI: 10.1063/1.2768953]

I. INTRODUCTION

The probability density function (PDF) approach has proven to be useful for large eddy simulation (LES) of turbulent reacting flows.[1,2] The formal means of conducting such LES is by considering the "filtered density function" (FDF).[3,4] The fundamental property of the FDF is to account for the effects of subgrid-scale (SGS) fluctuations in a probabilistic manner. Since its original conception,[3,4] the FDF has become very popular in the combustion research.[5] Most contributions thus far are based on the marginal scalar FDF (SFDF).[6–10] This popularity is due to the capacity of this formulation to provide a closed form for the chemical reaction effect. However, in the SFDF the effect of convection needs to be modeled similar to that in "conventional" LES. Gicquel *et al.*[11] developed the marginal FDF of the velocity vector (VFDF) in which the effect of SGS convection is in a closed form. However since the information about scalars is not embedded in the VFDF, this method is only suitable for constant-density, nonreacting flows. Following the developments as cited above, the FDF methodology has experienced widespread usage. Examples are contributions in its basic implementation,[12–23] fine-tuning of its subclosures,[24,25] and its validation via laboratory experiments.[26–30] The FDF is finding its way into commercial codes[31,32] and has been the subject of detailed discussions in several books.[1,33–35] Givi[2] provides a comprehensive review of the state of progress in LES/FDF.

The objective of the present work is to extend the FDF methodology to account for the "joint" SGS velocity and scalar fields in variable-density flows. This is accomplished by considering the joint "velocity-scalar filtered mass density function" (VSFMDF). This is the most comprehensive form of the FDF formulation to date. With the definition of the VSFMDF, the mathematical framework for its implementation in LES is established. A transport equation is developed for the VSFMDF in which the effects of SGS convection and chemical reaction (in a reacting flow) are in closed forms. The unclosed terms in this equation are modeled in a fashion similar to those in the Reynolds-averaged simulation (RAS)

[a]Author to whom correspondence should be addressed. Telephone: (412) 624-9755. Fax: (412) 624-4886. Electronic mail: moh3@pitt.edu

procedures. A Lagrangian Monte Carlo procedure is developed and implemented for numerical solution of the modeled VSFMDF transport equation. The consistency of this procedure is assessed by comparing the moments of the VSFMDF with those obtained by the Eulerian finite-difference of the same moments' transport equations. The results of the VSFMDF simulations are compared with those predicted by the Smagorinsky[36] closure. All the results are assessed via comparisons with direct numerical simulation (DNS) data of a three-dimensional (3D) temporally developing mixing layer involving transport of a passive scalar variable. The predictive capability of the VSFMDF methodology in reacting flows is assessed by comparison with experimental data of Mungal and Dimotakis[37] for a 3D reacting spatially developing mixing layer.

There have been significant previous investigations on the effect of density on turbulent flow[38–42] characteristics. These studies show how density changes modify the turbulent structures in both low-speed and high-speed flows. A significant effect is reduction of the shear layer growth rate which is due to modification of Reynolds stresses by density variations. Now that LES is becoming a viable tool for the simulation of turbulent reactive flows, it is useful to evaluate the ability of SGS models in accounting for variable density effects. In this study, such an evaluation is performed on the VSFMDF methodology. The shear layers considered in this study have low Mach number and hence, negligible compressibility effects. The spatial mixing layer simulations have moderate amounts of heat release with the density ratios of 1.3–1.5 for the range of concentration ratios considered. In the temporal mixing layer simulations, much higher free-stream density ratios (up to 8) are considered. These results are validated by comparing with DNS data of the same layer.

II. FORMULATION

In a turbulent flow undergoing chemical reactions involving N_s species, the primary transport variables are the density $\rho(\mathbf{x},t)$, the velocity vector $u_i(\mathbf{x},t)$ $(i=1,2,3)$, the pressure $p(\mathbf{x},t)$, the enthalpy $h(\mathbf{x},t)$ and the species' mass fractions $Y_\alpha(\mathbf{x},t)$ $(\alpha=1,2,\ldots,N_s)$. The equations which govern the transport of these variables in space (x_i) $(i=1,2,3)$ and time (t) are the continuity, momentum, enthalpy (energy), and species' mass fraction equations, along with an equation of state

$$\frac{\partial \rho}{\partial t}+\frac{\partial \rho u_j}{\partial x_j}=0, \tag{1a}$$

$$\frac{\partial \rho u_i}{\partial t}+\frac{\partial \rho u_j u_i}{\partial x_j}=-\frac{\partial p}{\partial x_i}+\frac{\partial \tau_{ji}}{\partial x_j}, \tag{1b}$$

$$\frac{\partial \rho \phi_\alpha}{\partial t}+\frac{\partial \rho u_j \phi_\alpha}{\partial x_j}=-\frac{\partial J_j^\alpha}{\partial x_j}+\rho S_\alpha, \quad \alpha=1,2,\ldots,\sigma=N_s+1, \tag{1c}$$

$$p=\rho R^0 T\sum_{\alpha=1}^{N_s} Y_\alpha/M_\alpha=\rho RT, \tag{1d}$$

where R^0 and R are the universal and mixture gas constants and M_α denotes the molecular weight of species α. The chemical reaction source terms $S_\alpha \equiv \hat{S}_\alpha(\boldsymbol{\phi}(\mathbf{x},t))$ are functions of compositional scalars $(\boldsymbol{\phi}\equiv[\phi_1,\phi_2,\ldots,\phi_{N_s+1}])$. Equation (1c) represents the transport of species' mass fraction and enthalpy in a common form with

$$\phi_\alpha \equiv Y_\alpha, \quad \alpha=1,2,\ldots,N_s, \quad \phi_\sigma \equiv h=\sum_{\alpha=1}^{N_s} h_\alpha \phi_\alpha, \tag{2}$$

and

$$h_\alpha=h_\alpha^0+\int_{T_0}^{T} c_{p_\alpha}(T')dT'. \tag{3}$$

Here T and T_0 denote the temperature field and the reference temperature, respectively. In this equation, h_α^0 and c_{p_α} denote the enthalpy of formation at T_0 and the specific heat at constant pressure for species α. For a Newtonian fluid, with Fick's law of diffusion, the viscous stress tensor τ_{ij} and the scalar flux J_j^α are represented by

$$\tau_{ij}=\mu\left(\frac{\partial u_i}{\partial x_j}+\frac{\partial u_j}{\partial x_i}-\frac{2}{3}\frac{\partial u_k}{\partial x_k}\delta_{ij}\right), \tag{4a}$$

$$J_j^\alpha=-\gamma\frac{\partial \phi_\alpha}{\partial x_j}, \tag{4b}$$

where μ is the fluid dynamic viscosity and $\gamma=\rho\Gamma$ denotes the thermal and mass molecular diffusivity coefficients for all the scalars. We assume $\mu=\gamma$, i.e., unity Schmidt (Sc) and Prandtl (Pr) numbers. The viscosity and molecular diffusivity coefficients can, in general, be temperature dependent but in this study, they are assumed to be constants. In reactive flows, molecular processes are much more complicated than portrayed by Eq. (4). Since the molecular diffusion is typically less important than that of SGS, this simple model is adopted with justifications and caveats given in Refs. 43–45.

Large eddy simulation involves the spatial filtering operation[1,46–49]

$$\langle f(\mathbf{x},t)\rangle_\ell=\int_{-\infty}^{+\infty} f(\mathbf{x}',t)G(\mathbf{x}',\mathbf{x})d\mathbf{x}', \tag{5}$$

where $G(\mathbf{x}',\mathbf{x})$ denotes a filter function, and $\langle f(\mathbf{x},t)\rangle_\ell$ is the filtered value of the transport variable $f(\mathbf{x},t)$. In variable-density flows it is convenient to use the Favre-filtered quantity $\langle f(\mathbf{x},t)\rangle_L=\langle \rho f\rangle_\ell/\langle \rho\rangle_\ell$. We consider a filter function that is spatially and temporally invariant and localized, thus $G(\mathbf{x}',\mathbf{x})\equiv G(\mathbf{x}'-\mathbf{x})$ with the properties $G(\mathbf{x})\geq 0$, $\int_{-\infty}^{+\infty}G(\mathbf{x})d\mathbf{x}=1$. Applying the filtering operation to Eqs. (1) and using the conventional LES approximation for the diffusion terms, we obtain

$$\frac{\partial\langle\rho\rangle_\ell}{\partial t}+\frac{\partial\langle\rho\rangle_\ell\langle u_j\rangle_L}{\partial x_j}=0, \tag{6a}$$

$$\frac{\partial\langle\rho\rangle_\ell\langle u_i\rangle_L}{\partial t}+\frac{\partial\langle\rho\rangle_\ell\langle u_j\rangle_L\langle u_i\rangle_L}{\partial x_j}=-\frac{\partial\langle p\rangle_\ell}{\partial x_i}+\frac{\partial}{\partial x_j}\left(\mu\left(\frac{\partial\langle u_i\rangle_L}{\partial x_j}+\frac{\partial\langle u_j\rangle_L}{\partial x_i}\right)\right)-\frac{2}{3}\frac{\partial}{\partial x_i}\left(\mu\frac{\partial\langle u_j\rangle_L}{\partial x_j}\right)-\frac{\partial\langle\rho\rangle_\ell\tau_L(u_i,u_j)}{\partial x_j}, \tag{6b}$$

$$\frac{\partial\langle\rho\rangle_\ell\langle\phi_\alpha\rangle_L}{\partial t}+\frac{\partial\langle\rho\rangle_\ell\langle u_j\rangle_L\langle\phi_\alpha\rangle_L}{\partial x_j}=\frac{\partial}{\partial x_j}\left(\mu\frac{\partial\langle\phi_\alpha\rangle_L}{\partial x_j}\right)-\frac{\partial\langle\rho\rangle_\ell\tau_L(u_j,\phi_\alpha)}{\partial x_j}+\left[\langle\rho\rangle_\ell\langle S_\alpha\rangle_L\right], \tag{6c}$$

where the second-order SGS correlations, defined by

$$\tau_L(a,b)=\langle ab\rangle_L-\langle a\rangle_L\langle b\rangle_L, \tag{7}$$

are governed by

$$\begin{aligned}\frac{\partial\langle\rho\rangle_\ell\tau_L(u_i,u_j)}{\partial t}+\frac{\partial\langle\rho\rangle_\ell\langle u_k\rangle_L\tau_L(u_i,u_j)}{\partial x_k}=&-\frac{\partial\langle\rho\rangle_\ell\tau_L(u_k,u_i,u_j)}{\partial x_k}-\langle\rho\rangle_\ell\tau_L(u_i,u_k)\frac{\partial\langle u_j\rangle_L}{\partial x_k}-\langle\rho\rangle_\ell\tau_L(u_j,u_k)\frac{\partial\langle u_i\rangle_L}{\partial x_k}+\frac{\partial}{\partial x_k}\left(\mu\frac{\partial\tau_L(u_i,u_j)}{\partial x_k}\right)\\&+\left[\tau_L\left(u_j,\frac{\partial}{\partial x_k}\left(\mu\frac{\partial u_k}{\partial x_i}\right)\right)+\tau_L\left(u_i,\frac{\partial}{\partial x_k}\left(\mu\frac{\partial u_k}{\partial x_j}\right)\right)\right]\\&-\frac{2}{3}\left[\tau_L\left(u_j,\frac{\partial}{\partial x_i}\left(\mu\frac{\partial u_k}{\partial x_k}\right)\right)+\tau_L\left(u_i,\frac{\partial}{\partial x_j}\left(\mu\frac{\partial u_k}{\partial x_k}\right)\right)\right]\\&-\left[\left(\left\langle u_j\frac{\partial p}{\partial x_i}\right\rangle_\ell-\langle u_j\rangle_L\frac{\partial\langle p\rangle_\ell}{\partial x_i}\right)+\left(\left\langle u_i\frac{\partial p}{\partial x_j}\right\rangle_\ell-\langle u_i\rangle_L\frac{\partial\langle p\rangle_\ell}{\partial x_j}\right)+2\mu\tau_L\left(\frac{\partial u_i}{\partial x_k},\frac{\partial u_j}{\partial x_k}\right)\right],\end{aligned} \tag{8a}$$

$$\begin{aligned}\frac{\partial\langle\rho\rangle_\ell\tau_L(u_i,\phi_\alpha)}{\partial t}+\frac{\partial\langle\rho\rangle_\ell\langle u_j\rangle_L\tau_L(u_i,\phi_\alpha)}{\partial x_j}=&-\frac{\partial\langle\rho\rangle_\ell\tau_L(u_j,u_i,\phi_\alpha)}{\partial x_j}-\langle\rho\rangle_\ell\tau_L(u_i,u_j)\frac{\partial\langle\phi_\alpha\rangle_L}{\partial x_j}-\langle\rho\rangle_\ell\tau_L(u_j,\phi_\alpha)\frac{\partial\langle u_i\rangle_L}{\partial x_j}\\&+\frac{\partial}{\partial x_j}\left(\mu\frac{\partial\tau_L(u_i,\phi_\alpha)}{\partial x_j}\right)+\left[\tau_L\left(\phi_\alpha,\frac{\partial}{\partial x_j}\left(\mu\frac{\partial u_j}{\partial x_i}\right)\right)-\frac{2}{3}\tau_L\left(\phi_\alpha,\frac{\partial}{\partial x_i}\left(\mu\frac{\partial u_j}{\partial x_j}\right)\right)\right]\\&-\left[\left(\left\langle\phi_\alpha\frac{\partial p}{\partial x_i}\right\rangle_\ell-\langle\phi_\alpha\rangle_L\frac{\partial\langle p\rangle_\ell}{\partial x_i}\right)+2\mu\tau_L\left(\frac{\partial u_i}{\partial x_j},\frac{\partial\phi_\alpha}{\partial x_j}\right)\right]+\left[\langle\rho\rangle_\ell\tau_L(u_i,S_\alpha(\boldsymbol{\phi}))\right],\end{aligned} \tag{8b}$$

$$\begin{aligned}\frac{\partial\langle\rho\rangle_\ell\tau_L(\phi_\alpha,\phi_\beta)}{\partial t}+\frac{\partial\langle\rho\rangle_\ell\langle u_i\rangle_L\tau_L(\phi_\alpha,\phi_\beta)}{\partial x_i}=&-\frac{\partial\langle\rho\rangle_\ell\tau_L(u_i,\phi_\alpha,\phi_\beta)}{\partial x_i}-\langle\rho\rangle_\ell\tau_L(\phi_\alpha,u_i)\frac{\partial\langle\phi_\beta\rangle_L}{\partial x_i}-\langle\rho\rangle_\ell\tau_L(\phi_\beta,u_i)\frac{\partial\langle\phi_\alpha\rangle_L}{\partial x_i}\\&+\frac{\partial}{\partial x_i}\left(\mu\frac{\partial\tau_L(\phi_\alpha,\phi_\beta)}{\partial x_i}\right)-\left[2\mu\tau_L\left(\frac{\partial\phi_\alpha}{\partial x_i},\frac{\partial\phi_\beta}{\partial x_i}\right)\right]\\&+\langle\rho\rangle_\ell[\tau_L(\phi_\alpha,S_\beta(\boldsymbol{\phi}))+\tau_L(\phi_\beta,S_\alpha(\boldsymbol{\phi}))].\end{aligned} \tag{8c}$$

In this equation, the third order correlations

$$\tau_L(a,b,c)=\langle abc\rangle_L-\langle a\rangle_L\tau_L(b,c)-\langle b\rangle_L\tau_L(a,c)-\langle c\rangle_L\tau_L(a,b)-\langle a\rangle_L\langle b\rangle_L\langle c\rangle_L \tag{9}$$

along with the other terms within square brackets are unclosed. Equations (6) and (8) provide an "exact" form of the transport equations.

III. VELOCITY-SCALAR FILTERED MASS DENSITY FUNCTION (VSFMDF)

A. Definitions

The "velocity-scalar filtered mass density function" (VSFMDF), denoted by P_L, is formally defined as[3]

$$P_L(\boldsymbol{v},\boldsymbol{\psi},\mathbf{x};t)=\int_{-\infty}^{+\infty}\rho(\mathbf{x}',t)\zeta(\boldsymbol{v},\boldsymbol{\psi};\boldsymbol{u}(\mathbf{x}',t),\boldsymbol{\phi}(\mathbf{x}',t))\times G(\mathbf{x}'-\mathbf{x})d\mathbf{x}', \tag{10}$$

where

$$\zeta(\boldsymbol{v},\boldsymbol{\psi};\boldsymbol{u}(\mathbf{x},t),\boldsymbol{\phi}(\mathbf{x},t))=\prod_{i=1}^{3}\delta(v_i-u_i(\mathbf{x},t))\times\prod_{\alpha=1}^{\sigma}\delta(\psi_\alpha-\phi_\alpha(\mathbf{x},t)). \tag{11}$$

In this equation, δ denotes the Dirac delta function, and $\boldsymbol{v},\boldsymbol{\psi}$

are the velocity vector and the scalar array in the sample space. The term ζ is the "fine-grained" density.[44,50] Equation (10) defines the VSFMDF as the spatially filtered value of the fine-grained density. With the condition of a positive filter kernel,[51] P_L has all of the properties of a mass density function (mdf).[44] For further developments it is useful to define the "conditional filtered value" of the variable $Q(\mathbf{x},t)$ as

$$\langle Q(\mathbf{x},t)|\boldsymbol{u}(\mathbf{x},t)=\boldsymbol{v},\boldsymbol{\phi}(\mathbf{x},t)=\boldsymbol{\psi}\rangle_\ell \equiv \langle Q|\boldsymbol{v},\boldsymbol{\psi}\rangle_\ell = \frac{\int_{-\infty}^{+\infty} Q(\mathbf{x}',t)\rho(\mathbf{x}',t)\zeta(\boldsymbol{v},\boldsymbol{\psi};\boldsymbol{u}(\mathbf{x}',t),\boldsymbol{\phi}(\mathbf{x}',t))G(\mathbf{x}'-\mathbf{x})d\mathbf{x}'}{P_L(\boldsymbol{v},\boldsymbol{\psi},\mathbf{x};t)}. \tag{12}$$

Equation (12) implies the following:

(i) for $Q(\mathbf{x},t)=c$, $\quad \langle Q(\mathbf{x},t)|\boldsymbol{v},\boldsymbol{\psi}\rangle_\ell = c$; (13a)

(ii) for $Q(\mathbf{x},t)\equiv \hat{Q}(\boldsymbol{u}(\mathbf{x},t),\boldsymbol{\phi}(\mathbf{x},t))$,

$$\langle Q(\mathbf{x},t)|\boldsymbol{v},\boldsymbol{\psi}\rangle_\ell = \hat{Q}(\boldsymbol{v},\boldsymbol{\psi}); \tag{13b}$$

(iii) integral properties:

$$\langle\rho(\mathbf{x},t)\rangle_\ell\langle Q(\mathbf{x},t)\rangle_L = \langle\rho(\mathbf{x},t)Q(\mathbf{x},t)\rangle_\ell = \int_{-\infty}^{+\infty}\int_{-\infty}^{+\infty}\langle Q(\mathbf{x},t)|\boldsymbol{v},\boldsymbol{\psi}\rangle_\ell \times P_L(\boldsymbol{v},\boldsymbol{\psi},\mathbf{x};t)d\boldsymbol{v}d\boldsymbol{\psi}. \tag{13c}$$

From Eqs. (13) it follows that the filtered value of any function of the velocity and/or scalar variables is obtained by its integration over the velocity and scalar sample spaces

$$\langle\rho(\mathbf{x},t)\rangle_\ell\langle Q(\mathbf{x},t)\rangle_L = \int_{-\infty}^{+\infty}\int_{-\infty}^{+\infty}\hat{Q}(\boldsymbol{v},\boldsymbol{\psi})P_L(\boldsymbol{v},\boldsymbol{\psi},\mathbf{x};t)d\boldsymbol{v}d\boldsymbol{\psi}. \tag{14}$$

B. VSFMDF transport equations

To develop the VSFMDF transport equation, we consider the time derivative of the fine-grained density function [Eq. (11)]

$$\frac{\partial\zeta}{\partial t} = -\left(\frac{\partial u_k}{\partial t}\frac{\partial\zeta}{\partial v_k} + \frac{\partial\phi_\alpha}{\partial t}\frac{\partial\zeta}{\partial\psi_\alpha}\right). \tag{15}$$

Substituting Eqs. (1b) and (1c), and Eqs. (4a) and (4b) into Eq. (15) we obtain

$$\frac{\partial\rho\zeta}{\partial t} + \frac{\partial\rho u_j\zeta}{\partial x_j} = \left(\frac{\partial p}{\partial x_j} - \frac{\partial\tau_{kj}}{\partial x_k}\right)\frac{\partial\zeta}{\partial v_j} + \left(\frac{\partial J_j^\alpha}{\partial x_j} - \rho S_\alpha(\boldsymbol{\phi})\right)\frac{\partial\zeta}{\partial\psi_\alpha}. \tag{16}$$

Integration of this equation according to Eq. (10), while employing Eq. (12) results in

$$\begin{aligned}\frac{\partial P_L}{\partial t} + \frac{\partial v_j P_L}{\partial x_j} = &-\frac{\partial}{\partial\psi_\alpha}(S_\alpha(\boldsymbol{\psi})P_L) \\ &+ \frac{\partial}{\partial v_i}\left(\left\langle\frac{1}{\rho(\boldsymbol{\phi})}\ \frac{\partial p}{\partial x_i}\middle|\boldsymbol{v},\boldsymbol{\psi}\right\rangle_\ell P_L\right) \\ &- \frac{\partial}{\partial v_i}\left(\left\langle\frac{1}{\rho(\boldsymbol{\phi})}\ \frac{\partial\tau_{ji}}{\partial x_j}\middle|\boldsymbol{v},\boldsymbol{\psi}\right\rangle_\ell P_L\right) \\ &+ \frac{\partial}{\partial\psi_\alpha}\left(\left\langle\frac{1}{\rho(\boldsymbol{\phi})}\ \frac{\partial J_i^\alpha}{\partial x_i}\middle|\boldsymbol{v},\boldsymbol{\psi}\right\rangle_\ell P_L\right).\end{aligned} \tag{17}$$

This is an exact transport equation and indicates that the effects of convection, the second term on the left-hand side (LHS), and chemical reaction, the first term on the right-hand side (RHS), appear in closed forms. The unclosed terms denote convective effects in the velocity-scalar sample space. Alternatively, the VSFMDF equation can be expressed as

$$\begin{aligned}\frac{\partial P_L}{\partial t} + \frac{\partial v_i P_L}{\partial x_i} = &\frac{\partial}{\partial x_i}\left(\mu\frac{\partial(P_L/\rho(\boldsymbol{\psi}))}{\partial x_i}\right) - \frac{\partial}{\partial\psi_\alpha}(S_\alpha(\boldsymbol{\psi})P_L) + \frac{\partial}{\partial v_i}\left[\left\langle\frac{1}{\rho(\boldsymbol{\phi})}\ \frac{\partial p}{\partial x_i}\middle|\mathbf{v},\boldsymbol{\psi}\right\rangle_\ell P_L\right] \\ &- \frac{\partial^2}{\partial v_i\,\partial v_j}\left[\left\langle\frac{\mu}{\rho(\boldsymbol{\phi})}\frac{\partial u_i}{\partial x_k}\ \frac{\partial u_j}{\partial x_k}\middle|\mathbf{v},\boldsymbol{\psi}\right\rangle_\ell P_L\right] - \frac{\partial}{\partial v_i}\left[\left\langle\frac{1}{\rho(\boldsymbol{\phi})}\frac{\partial}{\partial x_j}\left(\mu\frac{\partial u_j}{\partial x_i}\right)\middle|\mathbf{v},\boldsymbol{\psi}\right\rangle_\ell P_L\right] \\ &+ \frac{2}{3}\frac{\partial}{\partial v_i}\left[\left\langle\frac{1}{\rho(\boldsymbol{\phi})}\frac{\partial}{\partial x_i}\left(\mu\frac{\partial u_j}{\partial x_j}\right)\middle|\mathbf{v},\boldsymbol{\psi}\right\rangle_\ell P_L\right] - 2\frac{\partial^2}{\partial v_i\,\partial\psi_\alpha}\left[\left\langle\frac{\mu}{\rho(\boldsymbol{\phi})}\frac{\partial u_i}{\partial x_j}\ \frac{\partial\phi_\alpha}{\partial x_j}\middle|\mathbf{v},\boldsymbol{\psi}\right\rangle_\ell P_L\right] \\ &- \frac{\partial^2}{\partial\psi_\alpha\,\partial\psi_\beta}\left[\left\langle\frac{\mu}{\rho(\boldsymbol{\phi})}\frac{\partial\phi_\alpha}{\partial x_k}\frac{\partial\phi_\beta}{\partial x_k}\middle|\mathbf{v},\boldsymbol{\psi}\right\rangle_\ell P_L\right].\end{aligned} \tag{18}$$

This is also an exact equation. The unclosed terms are exhibited by the conditional filtered values as shown by the last six terms on the RHS.

C. Modeled VSFMDF transport equation

For closure of the VSFMDF transport equation, we consider the general diffusion process,[52] given by the system of stochastic differential equations (SDEs):

$$dX_i^+(t) = D_i^X(\mathbf{X}^+,\mathbf{U}^+,\boldsymbol{\phi}^+;t)dt + B_{ij}^X(\mathbf{X}^+,\mathbf{U}^+,\boldsymbol{\phi}^+;t)dW_j^X(t) + F_{ij}^{XU}(\mathbf{X}^+,\mathbf{U}^+,\boldsymbol{\phi}^+;t)dW_j^U(t) + F_{ij}^{X\phi}(\mathbf{X}^+,\mathbf{U}^+,\boldsymbol{\phi}^+;t)dW_j^\phi(t), \tag{19a}$$

$$dU_i^+(t) = D_i^U(\mathbf{X}^+,\mathbf{U}^+,\boldsymbol{\phi}^+;t)dt + B_{ij}^U(\mathbf{X}^+,\mathbf{U}^+,\boldsymbol{\phi}^+;t)dW_j^U(t) + F_{ij}^{UX}(\mathbf{X}^+,\mathbf{U}^+,\boldsymbol{\phi}^+;t)dW_j^X(t) + F_{ij}^{U\phi}(\mathbf{X}^+,\mathbf{U}^+,\boldsymbol{\phi}^+;t)dW_j^\phi(t), \tag{19b}$$

$$d\phi_\alpha^+(t) = D_\alpha^\phi(\mathbf{X}^+,\mathbf{U}^+,\boldsymbol{\phi}^+;t)dt + B_{\alpha j}^\phi(\mathbf{X}^+,\mathbf{U}^+,\boldsymbol{\phi}^+;t)dW_j^\phi(t) + F_{\alpha j}^{\phi X}(\mathbf{X}^+,\mathbf{U}^+,\boldsymbol{\phi}^+;t)dW_j^X(t) + F_{\alpha j}^{\phi U}(\mathbf{X}^+,\mathbf{U}^+,\boldsymbol{\phi}^+;t)dW_j^U(t), \tag{19c}$$

where X_i^+, U_i^+, ϕ_α^+ are probabilistic representations of position, velocity vector, and scalar variables, respectively. The D terms denote drift coefficient, the B terms denote diffusion, the F terms denote diffusion couplings, and the W terms denote the Wiener-Lévy processes.[53,54] To model these coefficients, following Refs. 9, 11, and 55–57 we utilize the simplified Langevin model (SLM) and the linear mean square estimation (LMSE) model[50]

$$dX_i^+ = U_i^+ dt + \sqrt{\frac{2\mu}{\langle\rho\rangle_\ell}}dW_i, \tag{20a}$$

$$dU_i^+ = \left[-\frac{1}{\langle\rho\rangle_\ell}\frac{\partial\langle p\rangle_\ell}{\partial x_i} + \frac{2}{\langle\rho\rangle_\ell}\frac{\partial}{\partial x_j}\left(\mu\frac{\partial\langle u_i\rangle_L}{\partial x_j}\right) + \frac{1}{\langle\rho\rangle_\ell}\frac{\partial}{\partial x_j}\left(\mu\frac{\partial\langle u_j\rangle_L}{\partial x_i}\right) - \frac{2}{3}\frac{1}{\langle\rho\rangle_\ell}\frac{\partial}{\partial x_i}\left(\mu\frac{\partial\langle u_j\rangle_L}{\partial x_j}\right)\right]dt + G_{ij}\left(U_j^+ - \langle u_j\rangle_L\right)dt + \sqrt{C_0\epsilon}dW_i' + \sqrt{\frac{2\mu}{\langle\rho\rangle_\ell}}\frac{\partial\langle u_i\rangle_L}{\partial x_j}dW_j, \tag{20b}$$

$$d\phi_\alpha^+ = -C_\phi\omega(\phi_\alpha^+ - \langle\phi_\alpha\rangle_L)dt + S_\alpha(\boldsymbol{\phi}^+)dt, \tag{20c}$$

where

$$G_{ij} = -\omega\left(\frac{1}{2}+\frac{3}{4}C_0\right)\delta_{ij}, \quad \omega = \frac{\epsilon}{k}, \qquad \epsilon = C_\epsilon\frac{k^{3/2}}{\Delta_L}, \quad k = \frac{1}{2}\tau_L(u_i,u_i). \tag{21}$$

Here ω is the SGS mixing frequency, ϵ is the dissipation rate, k is the SGS kinetic energy, and Δ_L is the LES filter size. The parameters C_0, C_ϕ, and C_ϵ are model constants and need to be specified. The Fokker-Planck equation[58] for $F_L(\boldsymbol{v},\boldsymbol{\psi},\mathbf{x};t)$, the joint PDF of $\mathbf{X}^+,\mathbf{U}^+,\boldsymbol{\phi}^+$, evolving by the diffusion process as given by Eq. (20) is

$$\frac{\partial F_L}{\partial t} + \frac{\partial v_i F_L}{\partial x_i} = \frac{1}{\langle\rho\rangle_\ell}\frac{\partial\langle p\rangle_\ell}{\partial x_i}\frac{\partial F_L}{\partial v_i} - \frac{2}{\langle\rho\rangle_\ell}\frac{\partial}{\partial x_j}\left(\mu\frac{\partial\langle u_i\rangle_L}{\partial x_j}\right)\frac{\partial F_L}{\partial v_i} - \frac{1}{\langle\rho\rangle_\ell}\frac{\partial}{\partial x_j}\left(\mu\frac{\partial\langle u_j\rangle_L}{\partial x_i}\right)\frac{\partial F_L}{\partial v_i} + \frac{2}{3}\frac{1}{\langle\rho\rangle_\ell}\frac{\partial}{\partial x_i}\left(\mu\frac{\partial\langle u_j\rangle_L}{\partial x_j}\right)\frac{\partial F_L}{\partial v_i} - G_{ij}\frac{\partial\left[\left(v_j-\langle u_j\rangle_L\right)F_L\right]}{\partial v_i} + \frac{\partial}{\partial x_j}\left(\mu\frac{\partial\left(F_L/\langle\rho\rangle_\ell\right)}{\partial x_j}\right) + \frac{\partial}{\partial x_j}\left(\frac{2\mu}{\langle\rho\rangle_\ell}\frac{\partial\langle u_i\rangle_L}{\partial x_j}\frac{\partial F_L}{\partial v_i}\right) + \frac{\mu}{\langle\rho\rangle_\ell}\frac{\partial\langle u_i\rangle_L}{\partial x_k}\frac{\partial\langle u_j\rangle_L}{\partial x_k}\frac{\partial^2 F_L}{\partial v_i\,\partial v_j} + \frac{1}{2}C_0\epsilon\frac{\partial^2 F_L}{\partial v_i\,\partial v_i} + C_\phi\omega\frac{\partial\left[\left(\psi_\alpha-\langle\phi_\alpha\rangle_L\right)F_L\right]}{\partial\psi_\alpha} - \frac{\partial\left(S_\alpha(\boldsymbol{\psi})F_L\right)}{\partial\psi_\alpha}. \tag{22}$$

Equation (20) governs the evolution of N_p notional particles, as explained in the subsequent section, which constitute a "stochastic particle system." This system has inherent different characteristics from the "fluid system" governed by Eq. (1).[1] Providing a perfect model, the stochastic particle system can, at most, give a statistical description of turbulence. In view of this limitation, we aim to make a correspondence between the two systems at the level of one-point, one-time statistics. This is done by equating the joint PDF of the particle system with the VSFMDF, i.e.,

$$F_L(\boldsymbol{v},\boldsymbol{\psi},\mathbf{x};t) = P_L(\boldsymbol{v},\boldsymbol{\psi},\mathbf{x};t). \tag{23}$$

The stochastic processes $\mathbf{X}^+(t)$, $\boldsymbol{U}^+(t)$, and $\boldsymbol{\phi}^+(t)$ are constructed in such a way that Eq. (23) is satisfied. This results in similarity of the statistics obtained from the two systems.

Because of this similarity, no distinction is made between these two statistics hereafter. The transport equations for the filtered variables are obtained by integration of Eq. (22) according to Eq. (14):

$$\frac{\partial\langle\rho\rangle_\ell}{\partial t}+\frac{\partial\langle\rho\rangle_\ell\langle u_j\rangle_L}{\partial x_j}=0, \tag{24a}$$

$$\begin{aligned}&\frac{\partial\langle\rho\rangle_\ell\langle u_i\rangle_L}{\partial t}+\frac{\partial\langle\rho\rangle_\ell\langle u_j\rangle_L\langle u_i\rangle_L}{\partial x_j}\\&=-\frac{\partial\langle p\rangle_\ell}{\partial x_i}+\frac{\partial}{\partial x_j}\left(\mu\left(\frac{\partial\langle u_i\rangle_L}{\partial x_j}+\frac{\partial\langle u_j\rangle_L}{\partial x_i}\right)\right)\\&\quad-\frac{2}{3}\frac{\partial}{\partial x_i}\left(\mu\frac{\partial\langle u_j\rangle_L}{\partial x_j}\right)-\frac{\partial\langle\rho\rangle_\ell\tau_L(u_i,u_j)}{\partial x_j},\end{aligned} \tag{24b}$$

$$\begin{aligned}&\frac{\partial\langle\rho\rangle_\ell\langle\phi_\alpha\rangle_L}{\partial t}+\frac{\partial\langle\rho\rangle_\ell\langle u_j\rangle_L\langle\phi_\alpha\rangle_L}{\partial x_j}\\&=\frac{\partial}{\partial x_j}\left(\mu\frac{\partial\langle\phi_\alpha\rangle_L}{\partial x_j}\right)-\frac{\partial\langle\rho\rangle_\ell\tau_L(\phi_\alpha,u_j)}{\partial x_j}\\&\quad+\langle\rho\rangle_\ell\langle S_\alpha(\boldsymbol{\phi})\rangle_L.\end{aligned} \tag{24c}$$

To have corresponding systems, the transport equations governing the systems should also correspond. From Eqs. (24), it is clear that the particle first order statistics satisfy the mass conservation as well as momentum and scalar transport equations. The transport equations for the second order SGS moments are

$$\begin{aligned}&\frac{\partial\langle\rho\rangle_\ell\tau_L(u_i,u_j)}{\partial t}+\frac{\partial\langle\rho\rangle_\ell\langle u_k\rangle_L\tau_L(u_i,u_j)}{\partial x_k}\\&=-\frac{\partial\langle\rho\rangle_\ell\tau_L(u_k,u_i,u_j)}{\partial x_k}+\frac{\partial}{\partial x_k}\left(\mu\frac{\partial\tau_L(u_i,u_j)}{\partial x_k}\right)\\&\quad-\langle\rho\rangle_\ell\tau_L(u_i,u_k)\frac{\partial\langle u_j\rangle_L}{\partial x_k}-\langle\rho\rangle_\ell\tau_L(u_j,u_k)\frac{\partial\langle u_i\rangle_L}{\partial x_k}\\&\quad+\langle\rho\rangle_\ell G_{ik}\tau_L(u_j,u_k)+\langle\rho\rangle_\ell G_{jk}\tau_L(u_i,u_k)+\langle\rho\rangle_\ell C_0\epsilon\delta_{ij},\end{aligned} \tag{25a}$$

$$\begin{aligned}&\frac{\partial\langle\rho\rangle_\ell\tau_L(u_i,\phi_\alpha)}{\partial t}+\frac{\partial\langle\rho\rangle_\ell\langle u_j\rangle_L\tau_L(u_i,\phi_\alpha)}{\partial x_j}\\&=-\frac{\partial\langle\rho\rangle_\ell\tau_L(u_j,u_i,\phi_\alpha)}{\partial x_j}+\frac{\partial}{\partial x_j}\left(\mu\frac{\partial\tau_L(u_i,\phi_\alpha)}{\partial x_j}\right)\\&\quad-\langle\rho\rangle_\ell\tau_L(u_i,u_j)\frac{\partial\langle\phi_\alpha\rangle_L}{\partial x_j}-\langle\rho\rangle_\ell\tau_L(u_j,\phi_\alpha)\frac{\partial\langle u_i\rangle_L}{\partial x_j}\\&\quad+\langle\rho\rangle_\ell G_{ij}\tau_L(u_j,\phi_\alpha)-\langle\rho\rangle_\ell C_\phi\omega\tau_L(u_i,\phi_\alpha)\\&\quad+\langle\rho\rangle_\ell\tau_L(u_i,S_\alpha(\boldsymbol{\phi})),\end{aligned} \tag{25b}$$

$$\begin{aligned}&\frac{\partial\langle\rho\rangle_\ell\tau_L(\phi_\alpha,\phi_\beta)}{\partial t}+\frac{\partial\langle\rho\rangle_\ell\langle u_i\rangle_L\tau_L(\phi_\alpha,\phi_\beta)}{\partial x_i}\\&=-\frac{\partial\langle\rho\rangle_\ell\tau_L(u_i,\phi_\alpha,\phi_\beta)}{\partial x_i}+\frac{\partial}{\partial x_i}\left(\mu\frac{\partial\tau_L(\phi_\alpha,\phi_\beta)}{\partial x_i}\right)\\&\quad-\langle\rho\rangle_\ell\tau_L(\phi_\alpha,u_i)\frac{\partial\langle\phi_\beta\rangle_L}{\partial x_i}-\langle\rho\rangle_\ell\tau_L(\phi_\beta,u_i)\frac{\partial\langle\phi_\alpha\rangle_L}{\partial x_i}\\&\quad+2\mu\frac{\partial\langle\phi_\alpha\rangle_L}{\partial x_i}\frac{\partial\langle\phi_\beta\rangle_L}{\partial x_i}-2\langle\rho\rangle_\ell C_\phi\omega\tau_L(\phi_\alpha,\phi_\beta)\\&\quad+\langle\rho\rangle_\ell\tau_L(\phi_\alpha,S_\beta(\boldsymbol{\phi}))+\langle\rho\rangle_\ell\tau_L(\phi_\beta,S_\alpha(\boldsymbol{\phi})).\end{aligned} \tag{25c}$$

The implied closure for the SDEs (20) is obtained by comparing the Fokker-Planck equation [Eq. (22)] to the VSFMDF transport equation [Eq. (18)]

$$\begin{aligned}&\frac{\partial}{\partial v_i}\left[\left\langle\frac{1}{\rho(\boldsymbol{\phi})}\frac{\partial p}{\partial x_k}\middle|\mathbf{v},\boldsymbol{\psi}\right\rangle_\ell P_L\right]-\frac{\partial^2}{\partial v_i\,\partial v_j}\left[\left\langle\frac{\mu}{\rho(\boldsymbol{\phi})}\frac{\partial u_i}{\partial x_k}\frac{\partial u_j}{\partial x_k}\middle|\mathbf{v},\boldsymbol{\psi}\right\rangle_\ell P_L\right]-\frac{\partial}{\partial v_i}\left[\left\langle\frac{1}{\rho(\boldsymbol{\phi})}\frac{\partial}{\partial x_j}\left(\mu\frac{\partial u_j}{\partial x_i}\right)\middle|\mathbf{v},\boldsymbol{\psi}\right\rangle_\ell P_L\right]\\&\quad+\frac{2}{3}\frac{\partial}{\partial v_i}\left[\left\langle\frac{1}{\rho(\boldsymbol{\phi})}\frac{\partial}{\partial x_i}\left(\mu\frac{\partial u_j}{\partial x_j}\right)\middle|\mathbf{v},\boldsymbol{\psi}\right\rangle_\ell P_L\right]-2\frac{\partial^2}{\partial v_i\,\partial\psi_\alpha}\left[\left\langle\frac{\mu}{\rho(\boldsymbol{\phi})}\frac{\partial u_i}{\partial x_j}\frac{\partial\phi_\alpha}{\partial x_j}\middle|\mathbf{v},\boldsymbol{\psi}\right\rangle_\ell P_L\right]\\&\quad-\frac{\partial^2}{\partial\psi_\alpha\,\partial\psi_\beta}\left[\left\langle\frac{\mu}{\rho(\boldsymbol{\phi})}\frac{\partial\phi_\alpha}{\partial x_i}\frac{\partial\phi_\beta}{\partial x_i}\middle|\mathbf{v},\boldsymbol{\psi}\right\rangle_\ell P_L\right]\\&=\frac{1}{\langle\rho\rangle_\ell}\frac{\partial\langle p\rangle_\ell}{\partial x_i}\frac{\partial F_L}{\partial v_i}-\frac{2}{\langle\rho\rangle_\ell}\frac{\partial}{\partial x_j}\left(\mu\frac{\partial\langle u_i\rangle_L}{\partial x_j}\right)\frac{\partial F_L}{\partial v_i}-\frac{1}{\langle\rho\rangle_\ell}\frac{\partial}{\partial x_j}\left(\mu\frac{\partial\langle u_j\rangle_L}{\partial x_i}\right)\frac{\partial F_L}{\partial v_i}+\frac{2}{3}\frac{1}{\langle\rho\rangle_\ell}\frac{\partial}{\partial x_i}\left(\mu\frac{\partial\langle u_j\rangle_L}{\partial x_j}\right)\frac{\partial F_L}{\partial v_i}\\&\quad-G_{ij}\frac{\partial\left[\left(v_j-\langle u_j\rangle_L\right)F_L\right]}{\partial v_i}+\frac{\partial}{\partial x_j}\left(\frac{2\mu}{\langle\rho\rangle_\ell}\frac{\partial\langle u_i\rangle_L}{\partial x_j}\frac{\partial F_L}{\partial v_i}\right)+\frac{\mu}{\langle\rho\rangle_\ell}\frac{\partial\langle u_i\rangle_L}{\partial x_k}\frac{\partial\langle u_j\rangle_L}{\partial x_k}\frac{\partial^2F_L}{\partial v_i\,\partial v_j}+\frac{1}{2}C_0\epsilon\frac{\partial^2F_L}{\partial v_i\,\partial v_i}\\&\quad+C_\phi\omega\frac{\partial\left[\left(\psi_\alpha-\langle\phi_\alpha\rangle_L\right)F_L\right]}{\partial\psi_\alpha}.\end{aligned} \tag{26}$$

The set of equations (24) and (25) may be compared with Eqs. (6) and (8). The closure at the second order level is

$$
\begin{aligned}
&-2\mu\tau_L\left(\frac{\partial u_i}{\partial x_k},\frac{\partial u_j}{\partial x_k}\right)+\tau_L\left(u_j,\frac{\partial}{\partial x_k}\left(\mu\frac{\partial u_k}{\partial x_i}\right)\right)\\
&\quad+\tau_L\left(u_i,\frac{\partial}{\partial x_k}\left(\mu\frac{\partial u_k}{\partial x_j}\right)\right)-\frac{2}{3}\tau_L\left(u_j,\frac{\partial}{\partial x_i}\left(\mu\frac{\partial u_k}{\partial x_k}\right)\right)\\
&\quad-\frac{2}{3}\tau_L\left(u_i,\frac{\partial}{\partial x_j}\left(\mu\frac{\partial u_k}{\partial x_k}\right)\right)-\left(\left\langle u_j\frac{\partial p}{\partial x_i}\right\rangle_\ell-\langle u_j\rangle_L\frac{\partial\langle p\rangle_\ell}{\partial x_i}\right)\\
&\quad-\left(\left\langle u_i\frac{\partial p}{\partial x_j}\right\rangle_\ell-\langle u_i\rangle_L\frac{\partial\langle p\rangle_\ell}{\partial x_j}\right)\\
&\quad\equiv\langle\rho\rangle_\ell G_{ik}\tau_L(u_j,u_k)+\langle\rho\rangle_\ell G_{jk}\tau_L(u_i,u_k)+\langle\rho\rangle_\ell C_0\epsilon\delta_{ij},
\end{aligned}
\tag{27a}
$$

$$
\begin{aligned}
&-2\mu\tau_L\left(\frac{\partial u_i}{\partial x_j},\frac{\partial\phi_\alpha}{\partial x_j}\right)+\tau_L\left(\phi_\alpha,\frac{\partial}{\partial x_j}\left(\mu\frac{\partial u_j}{\partial x_i}\right)\right)\\
&\quad-\frac{2}{3}\tau_L\left(\phi_\alpha,\frac{\partial}{\partial x_i}\left(\mu\frac{\partial u_j}{\partial x_j}\right)\right)\\
&\quad-\left(\left\langle\phi_\alpha\frac{\partial p}{\partial x_i}\right\rangle_\ell-\langle\phi_\alpha\rangle_L\frac{\partial\langle p\rangle_\ell}{\partial x_i}\right)\\
&\quad\equiv\langle\rho\rangle_\ell G_{ij}\tau_L(u_j,\phi_\alpha)-\langle\rho\rangle_\ell C_\phi\omega\tau_L(u_i,\phi_\alpha),
\end{aligned}
\tag{27b}
$$

$$
\begin{aligned}
\mu\tau_L\left(\frac{\partial\phi_\alpha}{\partial x_i},\frac{\partial\phi_\beta}{\partial x_i}\right)&\equiv\langle\rho\rangle_\ell C_\phi\omega\tau_L(\phi_\alpha,\phi_\beta)\\
&\quad-\mu\frac{\partial\langle\phi_\alpha\rangle_L}{\partial x_i}\frac{\partial\langle\phi_\beta\rangle_L}{\partial x_i}.
\end{aligned}
\tag{27c}
$$

It is clear that the transport equations implied by the model are consistent with the original LES equations [Eqs. (6) and (8)]. As indicated in Eq. (27c), in the scalar covariance equation, there is a spurious source term which is negligible at high Reynolds number flows.

IV. NUMERICAL SOLUTION PROCEDURE

Numerical solution of the modeled VSFMDF transport equation is obtained by a hybrid finite-difference/Monte Carlo procedure. The basis is similar to those in RAS (Refs. 59 and 60) and in previous FDF simulations,[9–11,57] with some differences which are described here. For simulations, the FDF is represented by an ensemble of N_p statistically identical Monte Carlo (MC) particles. Each particle carries information pertaining to its position, $\mathbf{X}^{(n)}(t)$, velocity, $\boldsymbol{U}^{(n)}(t)$, and scalar value, $\boldsymbol{\phi}^{(n)}(t)$, $n=1,\ldots,N_p$. This information is updated via temporal integration of the SDEs. The simplest way of performing this integration is via Euler-Maruyamma discretization.[61] For example, for Eq. (19a),

$$
\begin{aligned}
X_i^n(t_{k+1})&=X_i^n(t_k)+(D_i^X(t_k))^n\Delta t+(B_{ij}^X(t_k))^n(\Delta t)^{1/2}(\zeta_j^X(t_k))^n\\
&\quad+(F_{ij}^{XU}(t_k))^n(\Delta t)^{1/2}(\zeta_j^U(t_k))^n\\
&\quad+(F_{ij}^{X\phi}(t_k))^n(\Delta t)^{1/2}(\zeta_j^\phi(t_k))^n,
\end{aligned}
\tag{28}
$$

where $D_i(t_k)=D_i(\mathbf{X}^{(n)}(t_k),\boldsymbol{U}^{(n)}(t_k),\boldsymbol{\phi}^{(n)}(t_k);t_k)$, …, and $\zeta(t_k)$'s are independent standardized Gaussian random variables. This scheme preserves the Itô character of the SDEs.[62]

The computational domain is discretized on equally spaced finite-difference grid points. These points are used for three purposes: (1) to compute the pressure field, (2) to identify the regions where the statistical information from the MC simulations are obtained, and (3) to perform a set of complementary LES primarily by the finite-difference methodology for assessing the consistency and convergence of the MC results. The LES procedure via the finite-difference discretization is referred to as LES-FD and will be further discussed below. Statistical information is obtained by considering an ensemble of N_E computational particles residing within an ensemble domain of characteristic length Δ_E centered around each of the finite-difference grid points. For reliable statistics with minimal numerical dispersion, it is desired to minimize the size of an ensemble domain and maximize the number of the MC particles.[44] In this way, the ensemble statistics would tend to the desired filtered values,

$$
\begin{aligned}
\langle a\rangle_E&\equiv\frac{1}{N_E}\sum_{n\in\Delta_E}a^{(n)}\underset{\substack{N_E\to\infty\\ \Delta_E\to 0}}{\to}\langle a\rangle_L,\\
\tau_E(a,b)&\equiv\frac{1}{N_E}\sum_{n\in\Delta_E}(a^{(n)}-\langle a\rangle_E)(b^{(n)}-\langle b\rangle_E)\underset{\substack{N_E\to\infty\\ \Delta_E\to 0}}{\to}\tau_L(a,b),
\end{aligned}
\tag{29}
$$

where $a^{(n)}$ denotes the information carried by the nth MC particle pertaining to transport variable a.

To reduce the computational cost, a procedure involving the use of nonuniform weights[10] is also considered. This procedure allows a smaller number of particles in regions where a low degree of variability is expected. Conversely, in regions of high variability, a large number of particles is allowed. It has been shown[10,44] that the sum of weights within the ensemble domain is related to filtered fluid density as

$$
\langle\rho\rangle_\ell\approx\frac{\Delta m}{V_E}\sum_{n\in\Delta_E}w^{(n)},
\tag{30}
$$

where V_E is the volume of ensemble domain and Δm is the mass of particle with unit weight. The Favre-filtered value of a transport quantity $Q(\boldsymbol{v},\boldsymbol{\phi})$ is constructed from the weighted average as

$$
\langle Q\rangle_L\approx\frac{\Sigma_{n\in\Delta_E}w^{(n)}Q(\boldsymbol{v}^{(n)},\boldsymbol{\phi}^{(n)})}{\Sigma_{n\in\Delta_E}w^{(n)}}.
\tag{31}
$$

With uniform weights,[44] the particle number density decreases in regions of low density such as the reaction zone. The implementation of variable weights allows the increase in particle density without increasing the particle number density in these regions. The LES-FD solver is based on the compact parameter finite-difference scheme.[63,64] This is a variant of the MacCormack scheme in which fourth-order compact differencing schemes are used to approximate the spatial derivatives, and second-order symmetric predictor-corrector sequence is employed for time discretization. All of the finite-difference operations are conducted on fixed grid points. The transfer of information from the grid points to the MC particles is accomplished via a linear interpolation. The

transfer of information from the particles to the grid points is accomplished via ensemble averaging as described above.

The LES-FD procedure determines the pressure field which is further used in the MC solver. The transport equations to be solved by LES-FD solver include unclosed second order moments which are obtained from the MC solver. The LES-FD also determines the filtered velocity and scalar fields. That is, there is a "redundancy" in the determination of the first filtered moments as both the LES-FD and the MC procedures provide the solution of this field. This redundancy is actually very useful in monitoring the accuracy of the simulated results as shown in previous works.[10,11,57,59,60]

V. RESULTS

A. Flows simulated

The following flow configurations are considered:

(i) A three-dimensional temporally developing mixing layer involving transport of a passive scalar variable.
(ii) A three-dimensional spatially developing mixing layer involving chemical reaction with nonpremixed reactants.

Simulation (i) is used to assess the consistency and the overall capabilities of the VSFMDF methodology. This prediction is compared with data obtained by direct numerical simulation (DNS) of the same layer. Simulation (ii) is performed to demonstrate the predictive capabilities of the VSFMDF in reacting flows. The appraisal of these simulations is made by comparing to laboratory data.

In the representation below, x, y, and z denote the streamwise, the cross-stream, and the spanwise directions, respectively. The velocity components along these directions are denoted by u, v, and w in the x, y, and z directions, respectively. The temporal mixing layer consists of two parallel streams traveling in opposite directions with the same speed.[65–67] The filtered streamwise velocity, scalar and temperature fields are initialized with hyperbolic tangent profiles with free-stream conditions as $\langle u\rangle_L=1$, $\langle \phi\rangle_L=1$ on the top and $\langle u\rangle_L=-1$, $\langle \phi\rangle_L=0$ on the bottom. These simulations are performed with several density ratios defined as $s=\rho_1/\rho_2$ where ρ_1 and ρ_2 denote the $\langle\rho\rangle_\ell$ on the top and bottom free-streams, respectively. The density ratios of $s=1,2,4,8$ are considered. With the uniform initial pressure field, the initial $\langle T\rangle_L$ field is set equal to the inverse of $\langle\rho\rangle_\ell$ field based on ideal-gas equation of state. The length L_v is specified such that $L_v=2^{N_P}\lambda_u$, where N_P is the desired number of successive vortex pairings and λ_u is the wavelength of the most unstable mode corresponding to the mean streamwise velocity profile imposed at the initial time. The flow variables are normalized with respect to the half initial vorticity thickness, $L_r=[\delta_v(t=0)]/2$ $(\delta_v=\Delta U/|\partial\langle u\rangle_L/\partial y|_{\max}$, where $\langle u\rangle_L$ is the Reynolds-averaged value of the filtered streamwise velocity and ΔU is the velocity difference across the layer). The reference velocity is $U_r=\Delta U/2$.

Simulation (i) is conducted for a cubic box, $0\le x\le L$, $-L/2\le y\le L/2$, $0\le z\le L$ where $L=L_v/L_r$. The 3D field is parameterized in a procedure somewhat similar to that by Vreman *et al.*[68] The formation of the large scale structures are expedited through eigenfunction based initial perturbations.[69,70] This includes two-dimensional[66,68,71] and three-dimensional[66,72] perturbations with a random phase shift between the 3D modes. This results in the formation of two successive vortex pairings and strong three-dimensionality. The flow configuration in simulation (ii) is similar to the one considered in the laboratory experiments of Mungal and Dimotakis.[37] In these experiments, a heat-releasing reacting planar mixing layer consists of a low concentration of hydrogen (H_2) in one stream and a low concentration of fluorine (F_2) in the other stream. Both reactants are diluted in nitrogen (N_2) with the level of dilution determining the extent of heat release. The computational domain extends 54.8 cm $\times$ 36.6 cm $\times$ 4.6 cm in x, y, and z directions, respectively, which covers the whole region considered experimentally including $x=45.7$ cm where the measured data are reported. This flow is dominated by large scale two-dimensional structures.[38] Jaberi *et al.*[10] demonstrated the sufficiency of their two-dimensional simulations to capture hydrodynamic features of this flow and obtained good agreement with laboratory data. Therefore, to reduce the computational costs, the domain size in the z direction is considered to be minimal. It is shown that this size is sufficiently large to let three-dimensional large-scale structures develop. In order to simulate a "naturally" developing shear layer, a modified variant of the forcing procedure suggested in Ref. 73 is utilized. The cross-stream velocity component at the inlet is forced at the most unstable mode as well as four (sub- and super-) harmonics of this mode with a random phase shift. In these simulations, the variables are normalized by the values in the high-speed stream. The reference length $L_r=45.7$ cm which is the location in the experiment where the visual width of the layer is 7.4 cm.

Reaction mechanism

The chemical reaction considered in simulation (ii) involves the reaction of hydrogen (H_2) and fluorine (F_2) as represented by Dimotakis[37]

$$H_2 + F_2 \rightarrow 2HF, \quad \Delta Q = -130 \text{ kcal}^{-1} \text{ mol}^{-1}, \tag{32}$$

where ΔQ is the heat of reaction. This reaction is sufficiently energetic that 1% of F_2 and 1% of H_2 in nitrogen will produce an adiabatic flame temperature of 93 K above ambient. Thus, dilute concentrations produce significant temperature rise. The reaction actually consists of two second-order chain reactions with chemical times that are fast compared to the fluid mechanical time scales. Mungal and Dimotakis[37] indicate that for the conditions of the experiment, the H_2-F_2 mixture is in a stable region. Thus, for the chain reactions to proceed rapidly, it becomes crucial to provide some means to ensure the presence of F atoms. The technique used in the experiment consists of introducing a small amount of nitric oxide in the hydrogen reactant vessel. While it is necessary to add nitric oxide to initiate the reaction, the addition of excessive amounts would deplete the available F atoms. It was determined experimentally that by keeping the product of nitric oxide and fluorine concentrations at 0.03% the re-

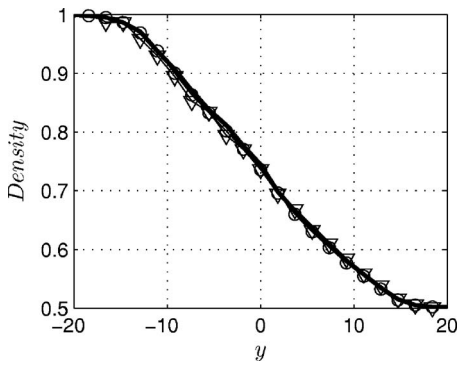

FIG. 1. Comparison of Reynolds-averaged values of different density estimates obtained from MC with LES-FD density ($\langle\rho\rangle_\ell$) in temporal mixing layer simulations with $s=2$ at $t=80$. The thick solid line denote LES-FD prediction. The symbols denote: (triangle) particle weight density [Eq. (30)] and (circle) MC density [Eq. (34)].

actions proceed rapidly. In this regard, it is important to note that the addition of 50% more nitric oxide showed no significant changes in the mean temperature profile. Thus, the chemistry can be considered to be relatively fast. This is also shown in Ref. 10 where they considered both finite-rate and fast chemistry models and observed negligible differences. Therefore, the fast chemistry model is considered here.

B. Numerical specifications

Simulations are conducted on equally spaced grid points. Simulation (i) has grid spacings $\Delta x=\Delta y=\Delta z=\Delta$ with the number of grid points 193^3 and 33^3 for DNS and LES, respectively. In this simulation the Reynolds number is $\mathrm{Re}=U_r L_r/\nu=50$. To filter the DNS data, a tophat function of the form below is used with $\Delta_L=2\,\Delta$,

$$G(\mathbf{x}'-\mathbf{x})=\prod_{i=1}^{3}\tilde{G}(x_i'-x_i), \tag{33}$$

$$\tilde{G}(x_i'-x_i)=\begin{cases}\dfrac{1}{\Delta_L}, & |x_i'-x_i|\le\dfrac{\Delta_L}{2},\\[2mm] 0, & |x_i'-x_i|>\dfrac{\Delta_L}{2}.\end{cases}$$

No attempt is made to investigate the sensitivity of the results to the filter function[51] or the size of the filter.[74]

Simulation (ii) is conducted on $81\times81\times12$ grid points in x, y, and z directions, respectively. The number of grid points in the z direction is sufficient and provides the same grid resolution as in y direction. The LES filter size in this simulation is $\Delta_L=2\Delta$ where $\Delta=(\Delta x\Delta y\Delta z)^{1/3}$. Hyperbolic tangent functions are utilized to assign the velocity, scalar, and temperature profiles for simulation (i), and at the inlet for simulation (ii). The same profiles are also used to initialize the particle values in both simulations and to assign the incoming particle values in simulation (ii). In simulation (ii), the characteristic boundary condition[75] is used at the inlet boundary. The pressure boundary condition[76] is used at the outflow boundary and a zero-derivative boundary condition is implemented at cross-stream boundaries.

All simulations are performed with variable particle weights.[10] In simulation (i), the MC particles are initially distributed throughout the computational region uniformly in a random fashion. The particle weights are set according to filtered fluid density at the initial time. In simulation (ii), the MC particles are initially distributed randomly within region $-0.15L_r\le y\le0.15L_r$ with a uniform distribution. In simulation (ii), the composition and velocity components of the incoming particles are the same as those in the experiment and consistent with those on LES grid points. The initial number of particles per grid point is NPG=320 ($N_E=40$) and the ensemble domain size (Δ_E) is set equal to half the grid spacing in each (x, y or z) direction. The effects of both of these parameters are assessed in the previous studies.[9–11,57] All results are analyzed both "instantaneously" and "statistically." In the former, the instantaneous contours (snapshots) and scatter plots of the variables of interest are analyzed. In the latter, the "Reynolds-averaged" statistics constructed from the instantaneous data are considered. These are constructed by spatial averaging over homogeneous directions

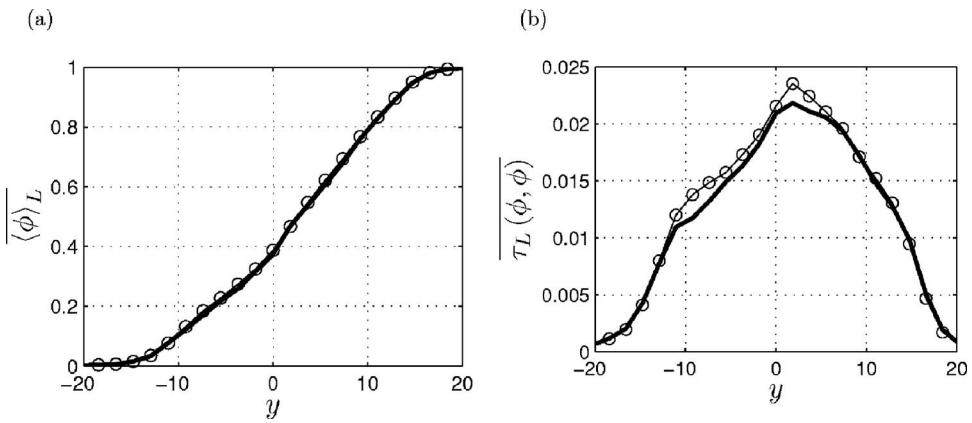

FIG. 2. Cross-stream variation of the Reynolds-averaged values of (a) $\langle\phi\rangle_L$, and (b) $\tau_L(\phi,\phi)$ in temporal mixing layer simulations at $t=80$ with $s=2$. The thick solid lines and circles denote LES-FD and MC predictions, respectively.

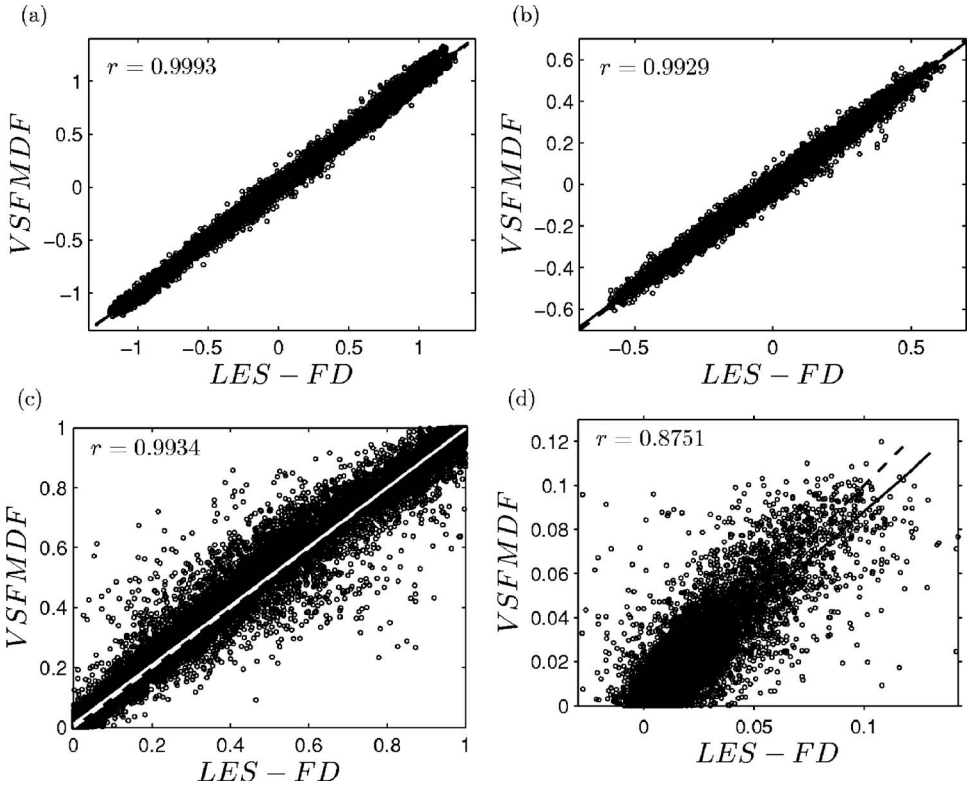

FIG. 3. Scatter plots of several velocity and scalar moments in temporal mixing layer simulations with $s=2$ at $t=80$. (a) $\langle u\rangle_L$, (b) $\langle v\rangle_L$, (c) $\langle \phi\rangle_L$, and (d) $\tau_L(\phi,\phi)$. The solid and dashed lines denote the linear regression and 45° lines, respectively. r denotes the correlation coefficient.

(x and z) in simulation (i) and by time averaging in simulation (ii). All Reynolds-averaged results are denoted by an overbar.

No attempt is made to determine the appropriate values of the model constants; the values suggested in the literature are adopted[77] $C_0=2.1$, $C_\epsilon=1$, and $C_\phi=1$. The influences of these parameters are assessed in Ref. 57. The value of Sc (=Pr) is 1 for all the simulations.

C. Consistency assessments

The objective of this section is to demonstrate the consistency of the VSFMDF formulation. Since the accuracy of the LES-FD procedure is well-established (at least for the first order filtered quantities), such a comparative assessment provides a good means of assessing the performance of the MC solution.

The uniformity of the MC particles is checked by monitoring their distributions at all times. The particle number density inside the ensemble domain (N_E) normalized by the initial N_E (here, initial $N_E=40$) varies around unity (as it should) while the particle weight density should be close to the filtered fluid density. The Reynolds-averaged density fields as obtained by both LES-FD and MC are shown in Fig. 1. As depicted, the particle weight density [see Eq. (30)] and the MC density, defined as

$$\langle \rho\rangle_E \equiv \left(\frac{\Sigma_{n\in\Delta_E} w^{(n)}(RT^{(n)}/\langle p\rangle_\ell)}{\Sigma_{n\in\Delta_E} w^{(n)}}\right)^{-1}, \tag{34}$$

are in very good agreement with the filtered density obtained from LES-FD.

The consistency is checked for the first two moments. As Fig. 2(a) shows, the cross-stream variation of filtered scalar is consistently predicted by LES-FD and MC. The same consistency is also observed for all other first moments. These

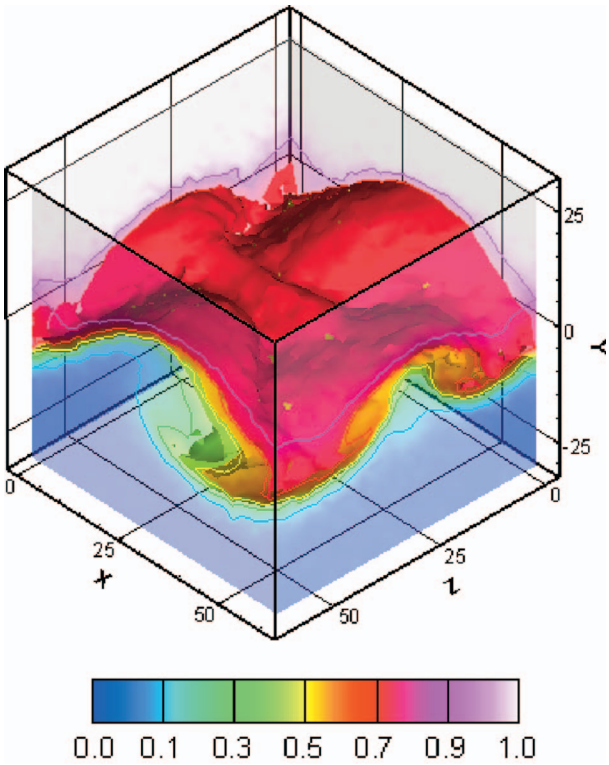

FIG. 4. (Color) Contour surfaces of the instantaneous $\langle \phi\rangle_L$ field in temporal mixing layer simulations with $s=2$ obtained from VSFMDF at $t=80$.

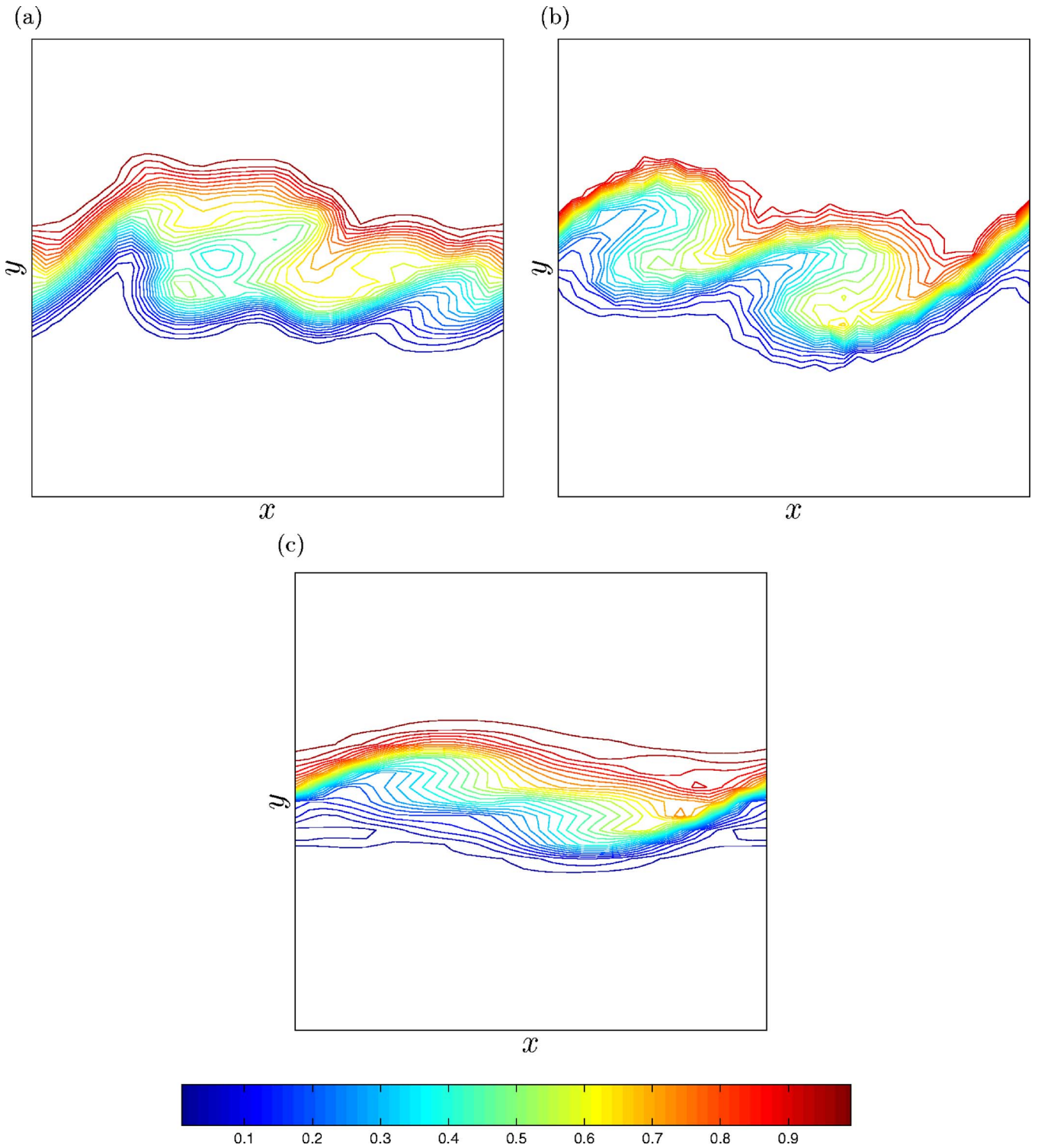

FIG. 5. (Color online) Contour plots of the $\langle\phi\rangle_L$ field on a spanwise plane at $z=0.75L$, $t=80$ in 3D temporal mixing layer simulations with $s=2$ as obtained by: (a) DNS (filtered), (b) VSFMDF, and (c) Smagorinsky.

moments show very little dependence on the values of Δ_E and N_E consistent with previous FDF simulations.[9–11,57] The consistency of the second order scalar correlation is also shown in Fig. 2(b). The predictions via MC show close agreement with LES-FD (the differences are due to statistical errors). With N_E and Δ_E chosen, this demonstration is consistent with previous assessment studies on the scalar,[9,10] the velocity,[11] and the velocity-scalar FDFs.[57] All other second order SGS moments behave similarly.

Complementary consistency assessment is obtained by presenting the scatter plots of instantaneous results obtained from LES-FD and MC. Figures 3(a) and 3(b) show the scat-

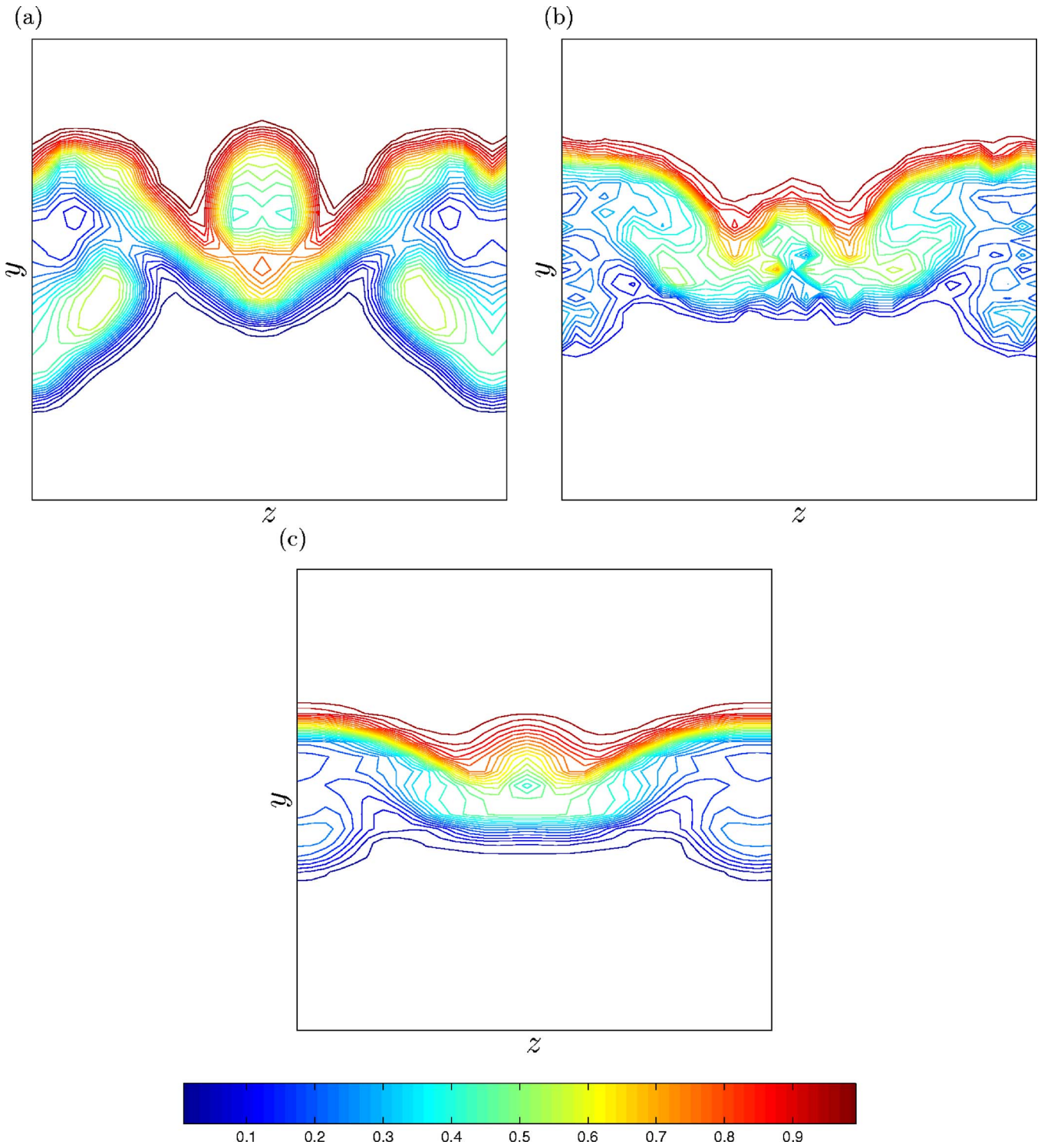

FIG. 6. (Color online) Contour plots of the $\langle\phi\rangle_L$ field on a streamwise plane at $x=0.25L$, $t=80$ in 3D temporal mixing layer simulations with $s=2$ as obtained by: (a) DNS (filtered), (b) VSFMDF, and (c) Smagorinsky.

ter plots of the velocity components in streamwise and cross-stream directions. For all the velocity components, there is a high level of correlation between LES-FD and MC results. In Fig. 3(c), the consistency of the filtered passive scalar field is demonstrated. For all the first order moments the linear regression line almost coincides with the 45° line. The scatter plot of scalar correlation is shown in Fig. 3(d). As shown, the scalar correlation shows increased statistical variations and hence, decreased correlation coefficient. The high level of correlations for all these quantities further establishes the consistency of the VSFMDF methodology.

D. Validation via DNS data

The objective of this section is to analyze some of the characteristics of the VSFMDF via comparative assessments

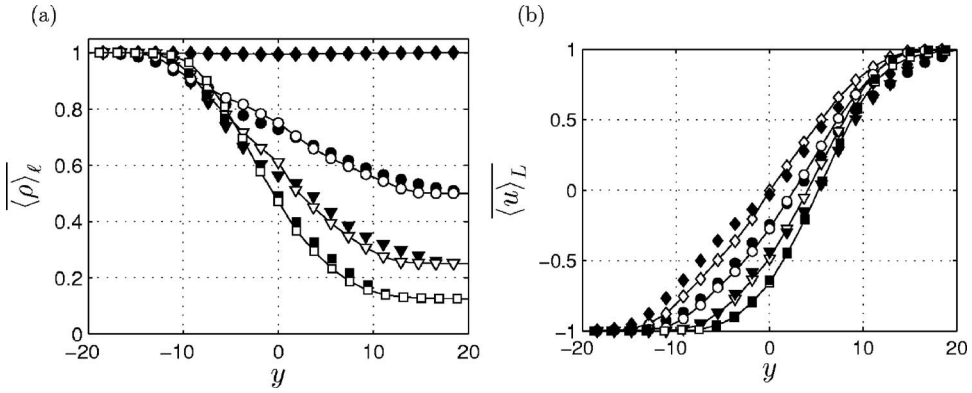

FIG. 7. Cross-stream variation of Reynolds-averaged (a) density, and (b) streamwise velocity at $t=80$ in temporal mixing layer simulations. The solid lines with white symbols denote VSFMDF predictions. The black symbols denote DNS predictions. The symbols denote: (diamond) $s=1$; (circle) $s=2$; (triangle) $s=4$; and (square) $s=8$.

against DNS of a three-dimensional temporal mixing layer. In addition, comparisons are also made with LES via the "conventional" Smagorinsky[36,78] model

$$\tau_L(u_i,u_j) = -2\nu_t\left(S_{ij} - \tfrac{1}{3}S_{nn}\delta_{ij}\right) + \tfrac{2}{3}k\delta_{ij},$$

$$\tau_L(u_i,\phi) = -\Gamma_t\frac{\partial\langle\phi\rangle_L}{\partial x_i},$$

$$S_{ij} = \frac{1}{2}\left(\frac{\partial\langle u_i\rangle_L}{\partial x_j} + \frac{\partial\langle u_j\rangle_L}{\partial x_i}\right), \tag{35}$$

$$\nu_t = C_\nu\Delta_L^2 S, \quad \Gamma_t = \frac{\nu_t}{Sc_t},$$

$C_\nu=0.04$, $\mathrm{Sc}_t=1$, $S=\sqrt{S_{ij}S_{ij}}$ and Δ_L is the characteristic length of the filter. The isotropic part of SGS stress is expressed using Yoshizawa's[79] expression

$$k = C_I\Delta_L^2 S^2. \tag{36}$$

Yoshizawa's constant of $C_I=0.18$ is adopted from the dynamic simulations of Moin *et al.*[80]

For comparison, the DNS data are filtered from the original high resolution 193^3 points to the coarse 33^3 points. In the comparisons, we also consider the "resolved" and the "total" components of the Reynolds-averaged moments. The former are denoted by $\overline{R(a,b)}$ with $R(a,b)=(\langle a\rangle_L-\overline{\langle a\rangle_L})\times(\langle b\rangle_L-\overline{\langle b\rangle_L})$; and the latter is $\overline{r(a,b)}$ with $r(a,b)=(a-\bar{a})\times(b-\bar{b})$. In DNS, the "total" components are directly available, while in LES they are approximated by $\overline{r(a,b)}\approx\overline{R(a,b)}+\overline{\tau_L(a,b)}$.[68]

Figure 4 shows the instantaneous isosurface of the $\langle\phi\rangle_L$ field at $t=80$. By this time, the flow is going through pairings and exhibits strong 3D effects. This is evident by the formation of large scale spanwise rollers with the presence of secondary structures in streamwise planes,[69] as also illustrated in Figs. 5 and 6. These figures show the scalar fields obtained from DNS, VSFMDF, and the Smagorinsky model on planes in the spanwise and streamwise directions. As Fig. 5 shows, the two neighboring rollers are being paired and in Fig. 6, the formation of secondary structures is evident. As illustrated in these figures and consistent with the previous works,[11] the results obtained from the Smagorinsky closure are overly smooth. This is due to the excessive amount of SGS diffusion with the Smagorinsky model. As shown, there is more resemblance in structures predicted by VSFMDF and DNS.

The effect of density variations on turbulence is studied in simulation (i). Free-stream density ratios of $s=1,2,4,8$ are considered in both VSFMDF and DNS. Figure 7(a) shows the filtered fluid density field as predicted by VSFMDF and DNS. The level of agreement between VSFMDF and DNS is satisfactory. The streamwise velocity fields predicted by VSFMDF and DNS are shown in Fig. 7(b) for selected density ratios. This figure exhibits the generally good agreement between VSFMDF and DNS results. In addition, it is also indicative of the accurate prediction of shear layer center location by VSFMDF. As the density ratio increases, the shear layer center, defined as the dividing streamline position (the position where $\overline{\langle u\rangle_L}$ is equal to the average of the free stream velocities), is shifted further to the low-density side. As a result, the peak values of the Reynolds stresses and scalar fluxes also show a shift to the low-density side. This shift is known to be responsible for the decreased correlation between density and velocity components[39] and hence, reduction in turbulent production terms. The growth rate of a temporally developing mixing layer is proportional to the integrated turbulent production terms.[81] Therefore, decrease in turbulent production results in reduction of shear layer growth rate. This is evidenced in Fig. 8 which shows the temporal evolution of the momentum thickness defined as[81]

$$\delta(t) = \frac{1}{\rho_1(\Delta u)^2}\int_{-\infty}^{+\infty}\overline{\langle\rho\rangle_\ell}(u_1-\overline{\langle u\rangle_L})(\overline{\langle u\rangle_L}-u_2)dy, \tag{37}$$

where $\Delta u=u_1-u_2$, u_1 and u_2 are top and bottom free-stream streamwise velocity components, respectively. As shown, the

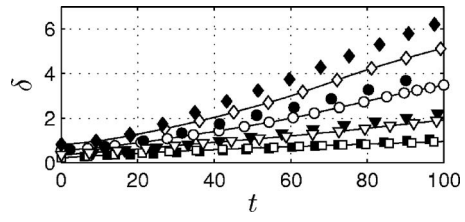

FIG. 8. Temporal variation of the momentum thickness in temporal mixing layer simulations. The solid lines with white symbols denote the VSFMDF predictions. The black symbols denote DNS predictions. The symbols denote: (diamond) $s=1$; (circle) $s=2$; (triangle) $s=4$; and (square) $s=8$.

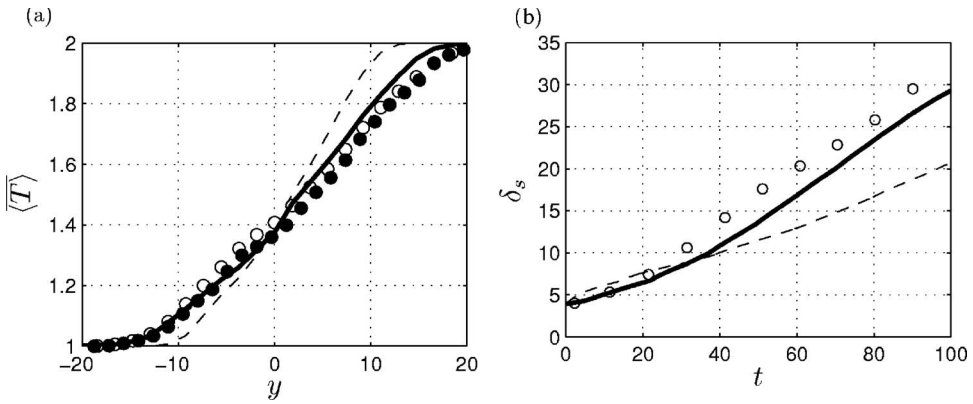

FIG. 9. (a) Cross-stream variation of the Reynolds-averaged values of the filtered temperature field at $t=80$, and (b) temporal variation of scalar thickness in temporal mixing layer simulations with $s=2$. The thick solid and thin dashed lines denote LES predictions using VSFMDF and Smagorinsky closures, respectively. The white and black circles show the filtered and unfiltered DNS data, respectively.

shear layer growth rate reduction with density ratio is represented well by VSFMDF.

The following comparative assessments of VSFMDF are shown for the density ratio of $s=2$. Similar agreement is observed for cases with other density ratios (but are not shown). The Reynolds-averaged values of the filtered temperature field at $t=80$ are shown in Fig. 9(a). The filtered and unfiltered DNS data yield virtually indistinguishable results. The Smagorinsky model underpredicts the spread of the layer due to dissipative nature of this model. All VSFMDF predictions compare well with DNS data in predicting the spread of the layer. This is also evident in Fig. 9(b) which shows the temporal variation of the "scalar thickness,"

$$\delta_s(t) = |y(\overline{\langle\phi\rangle}_L = 0.9)| + |y(\overline{\langle\phi\rangle}_L = 0.1)|. \quad (38)$$

Several components of the Reynolds-averaged values of the second order SGS moments are compared with DNS data in Figs. 10 and 11. In general, the VSFMDF results are in better agreement with DNS data than those predicted by the Smagorinsky model. In this configuration, there are no strong velocity and scalar gradients in the streamwise and spanwise directions and hence, a gradient-diffusion type model such as Smagorinsky is not capable of providing the correct prediction of scalar flux values in these directions. Consequently, the VSFMDF is expected to be more effective for LES of reacting flows provided that the extent of SGS mixing is heavily influenced by these SGS moments.[82,83]

Several components of the resolved second order moments are presented in Figs. 12 and 13. As expected, the performance of the Smagorinsky model is not satisfactory as it does not predict the spread and peak values accurately. The VSFMDF provides more reasonable predictions. The "total" components also yield very good agreement with DNS data as shown in Figs. 14 and 15. The effects of model parameters are assessed in Refs. 11 and 57. It is important to note that the first and the "total" second order moments predicted by

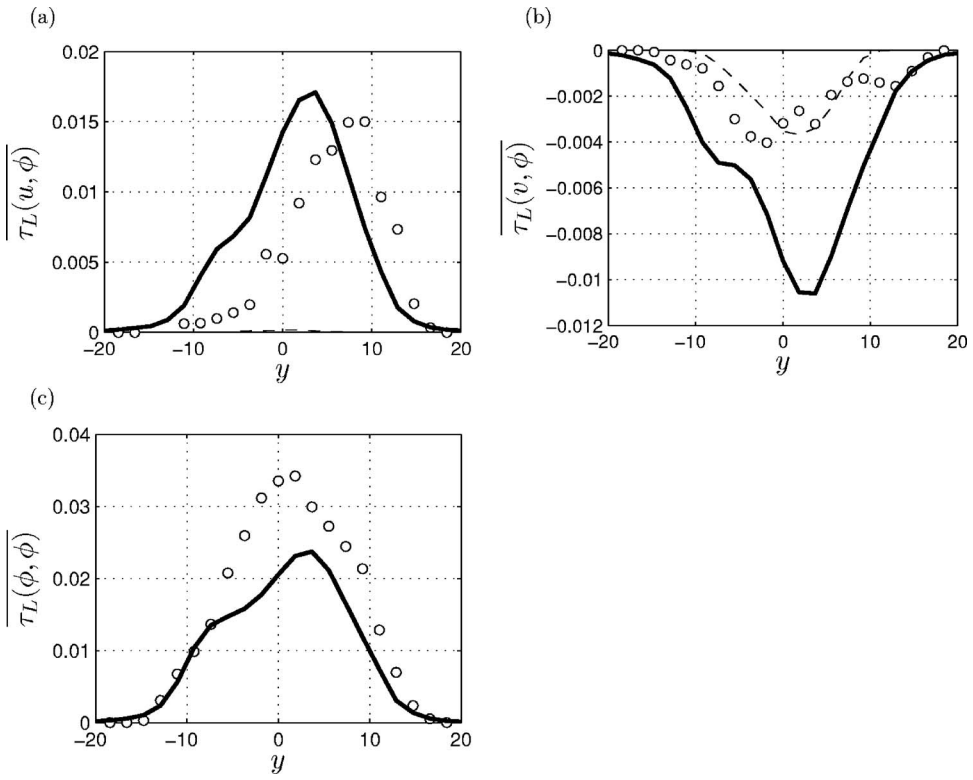

FIG. 10. Cross-stream variation of some of the Reynolds-averaged components of τ_L at $t=60$ in temporal mixing layer simulations with $s=2$. The thick solid and thin dashed lines denote LES predictions using VSFMDF and Smagorinsky closures, respectively. The circles show the filtered DNS data.

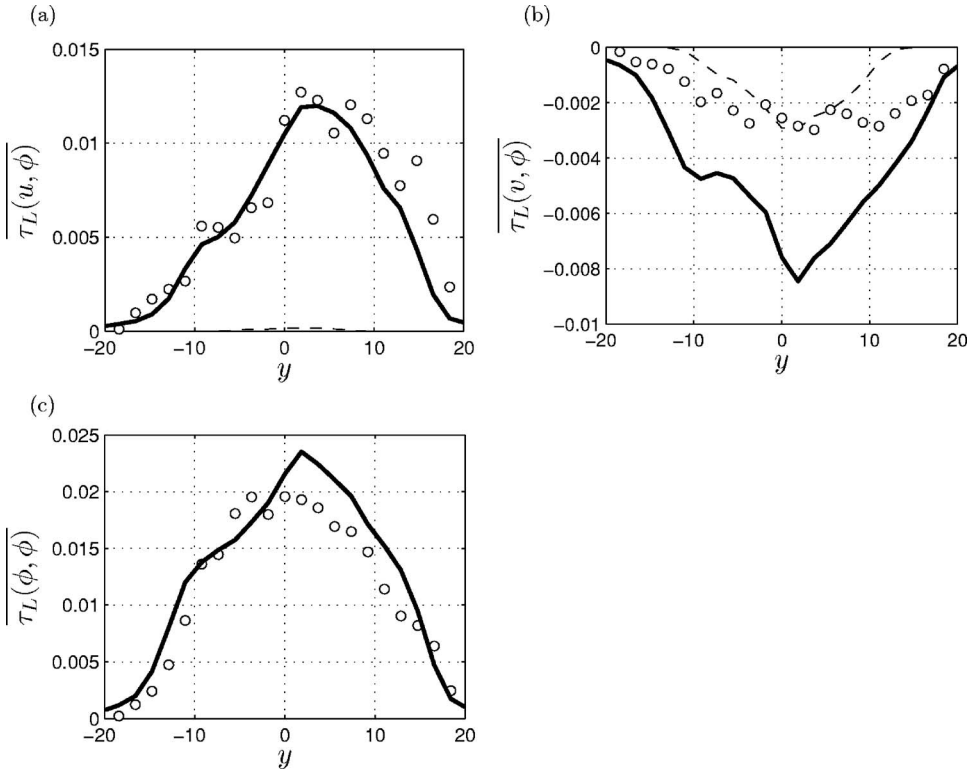

FIG. 11. Cross-stream variation of some of the Reynolds-averaged components of τ_L at $t=80$ in temporal mixing layer simulations with $s=2$. The thick solid and thin dashed lines denote LES predictions using VSFMDF and Smagorinsky closures, respectively. The circles show the filtered DNS data.

VSFMDF are almost insensitive to these parameters. This is pleasing because these are the quantities we are primarily interested in when comparing with experimental data, etc. Obviously, the values cannot be set in such a way that the contribution of the SGS components to the total components becomes too large. With the constant values chosen for VSFMDF, while the SGS scalar flux in cross-stream direction predicted by Smagorinsky is in closer agreement with DNS data, VSFMDF yields much more accurate predictions of the resolved and consequently, the total fields.

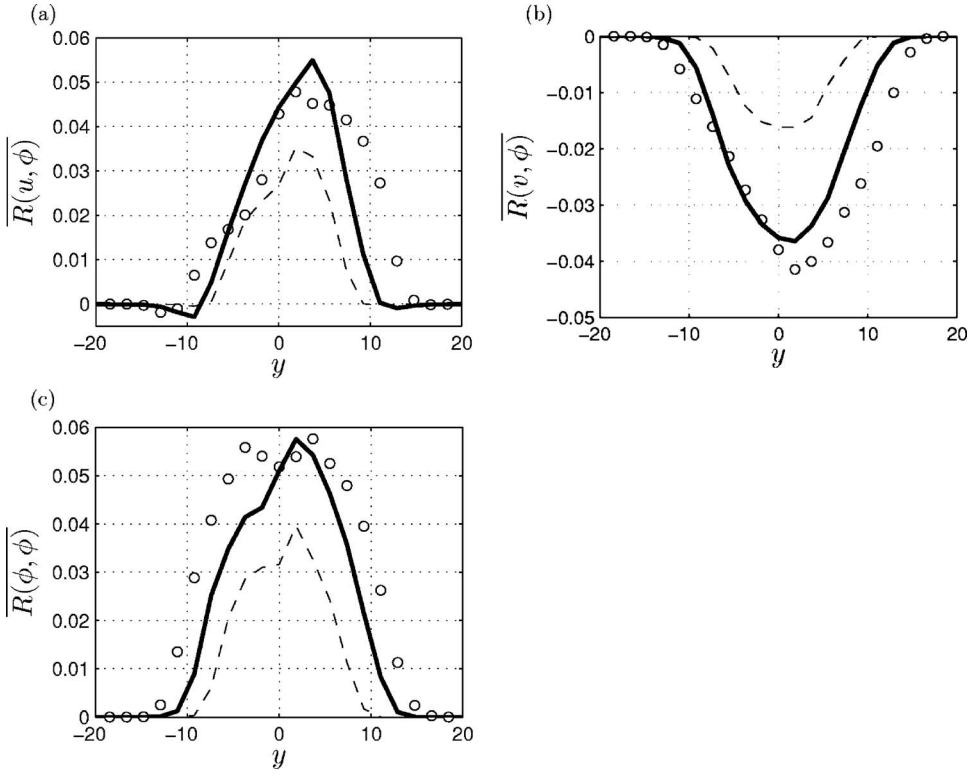

FIG. 12. Cross-stream variation of some of the components of $\bar{R}$ at $t=60$ in temporal mixing layer simulations with $s=2$. The thick solid and thin dashed lines denote LES predictions using VSFMDF and Smagorinsky closures, respectively. The circles show the filtered DNS data.

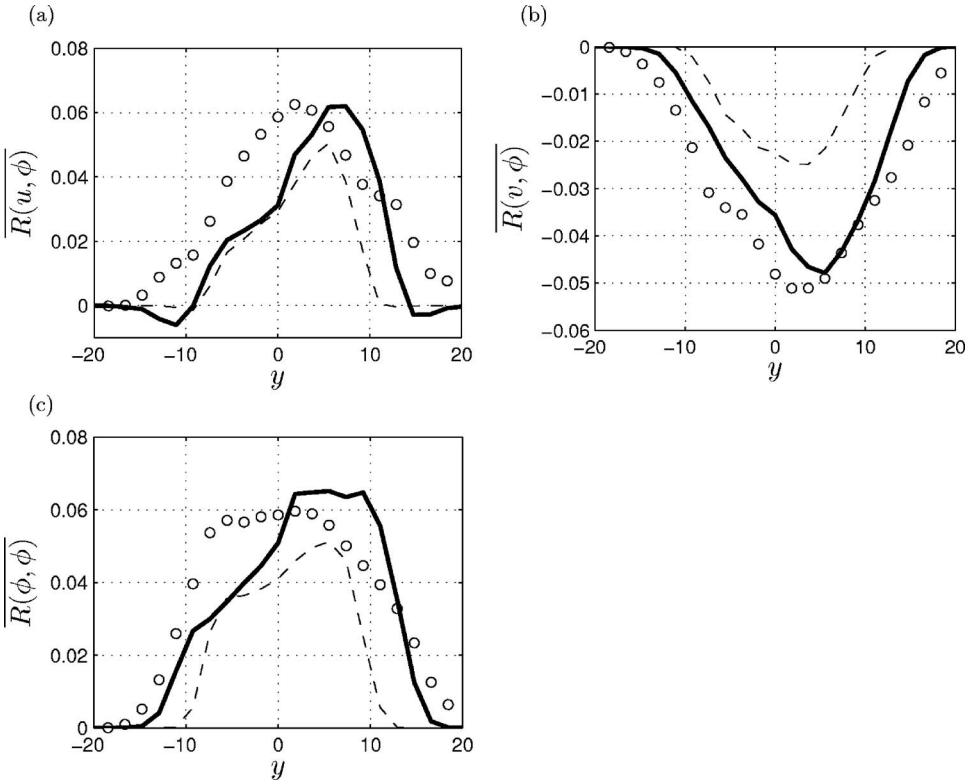

FIG. 13. Cross-stream variation of some of the components of $\bar{R}$ at $t=80$ in temporal mixing layer simulations with $s=2$. The thick solid and thin dashed lines denote LES predictions using VSFMDF and Smagorinsky closures, respectively. The circles show the filtered DNS data.

E. Validation via laboratory data

Simulation (ii) is consistent with the experimental studies of Mungal and Dimotakis.[37] These experiments are conducted with several concentration ratios, defined as $\phi = c_{02}/c_{01}$ where c_{01} and c_{02} denote the high- and low-speed stream mole fractions, respectively. In the current simulations, the concentration ratios of $\phi=1,2,4$ are considered by keeping F_2 concentration at 1% and varying the H_2 concentration from 1% to 2% and 4%. In addition, the flip experiments are also considered in which the low- and high-speed

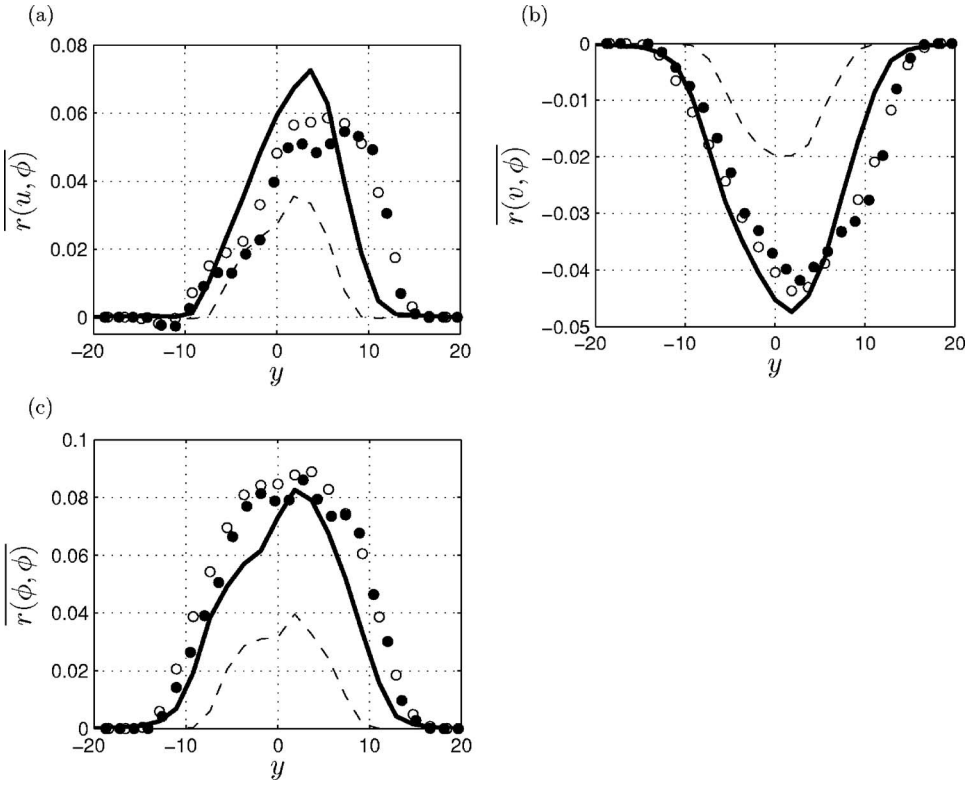

FIG. 14. Cross-stream variation of $\bar{r}$ at $t=60$ in temporal mixing layer simulations with $s=2$. The thick solid and thin dashed lines denote LES predictions using VSFMDF and Smagorinsky closures, respectively. The white and black circles show the filtered and unfiltered DNS data, respectively.

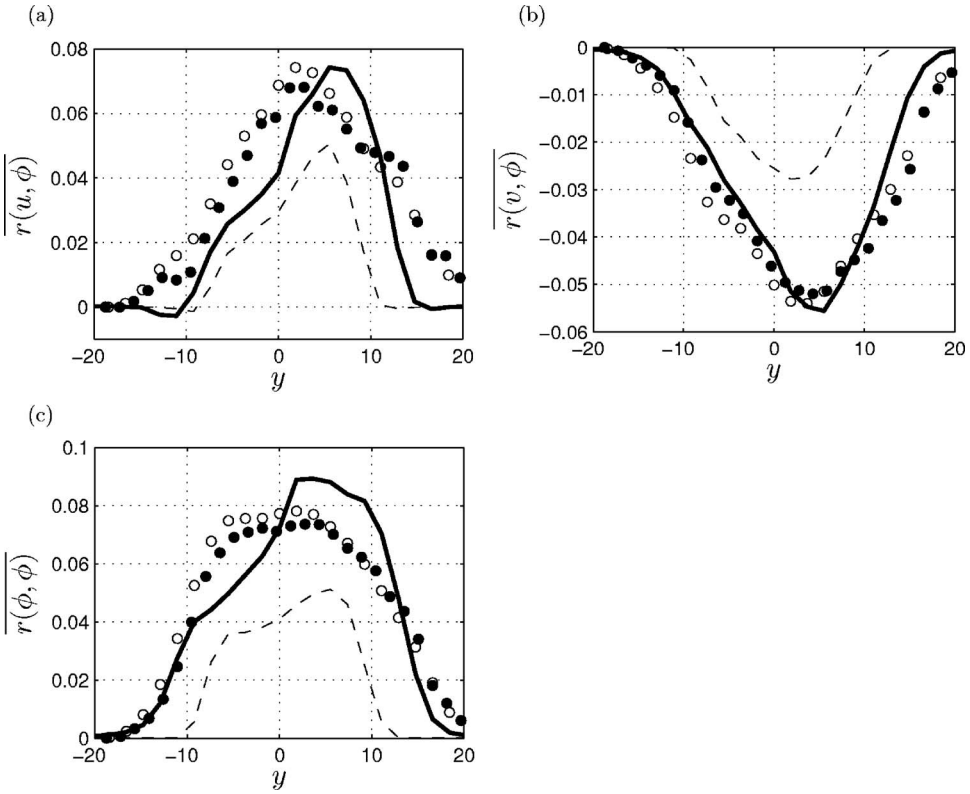

FIG. 15. Cross-stream variation of $\bar{r}$ at $t=80$ in temporal mixing layer simulations with $s=2$. The thick solid and thin dashed lines denote LES predictions using VSFMDF and Smagorinsky closures, respectively. The white and black circles show the filtered and unfiltered DNS data, respectively.

compositions are simply switched to attain the inverse concentration ratios ($\phi=1, 1/2, 1/4$). These simulations are conducted only via VSFMDF, as implementation of DNS and LES-FD is not possible for this flow.

The three-dimensionality of the flow is evident by the presence of primary and secondary structures, as shown in Fig. 16(a). This figure shows the contour surfaces of the instantaneous filtered scalar field. Figures 16(b) and 16(c) show the instantaneous temperature field as obtained by LES-FD and VSFMDF. The resemblance of structures in these figures, is an indication of the consistency of these simulations. The time series of the filtered temperature field recorded by 15 probes across the layer, are shown in Fig. 17(a). These probes are located at $x=45.7$ cm downstream and are symmetrically distributed in cross-stream direction about the centerline with the vertical distance of 0.457 cm between each two. The high-speed stream located on top and carries 1% H_2 and the low-speed stream is in the bottom with 1% F_2 composition. In this figure, the horizontal axis corresponds to the nondimensional time starting at one flow-through time. The vertical axis for each section represents the temperature ranging from the ambient to the maximum temperature recorded by each probe (denoted as $T_{\max}$). Several features observed experimentally[37] are also present in these time series, namely, the presence of large, hot structures; the cold regions extending deep into the layer and the near-uniformity of temperature within the structure. The non-uniformity of temperatures in previous simulations[10] was attributed to the lack of proper small-scale mixing due to two-dimensionality of their simulations. The present simulations substantiate this, as the more effective small-scale mixing in three-dimensional simulations tends to make the temperature more uniform inside the structures. Figure 17(b) shows a comparison of VSFMDF predictions with experimental data. The time-averaged filtered temperature profile corresponding to the case with concentration ratio $\phi=1$ is considered. The peak value of the temperature profile and the spread of layer are both predicted well.

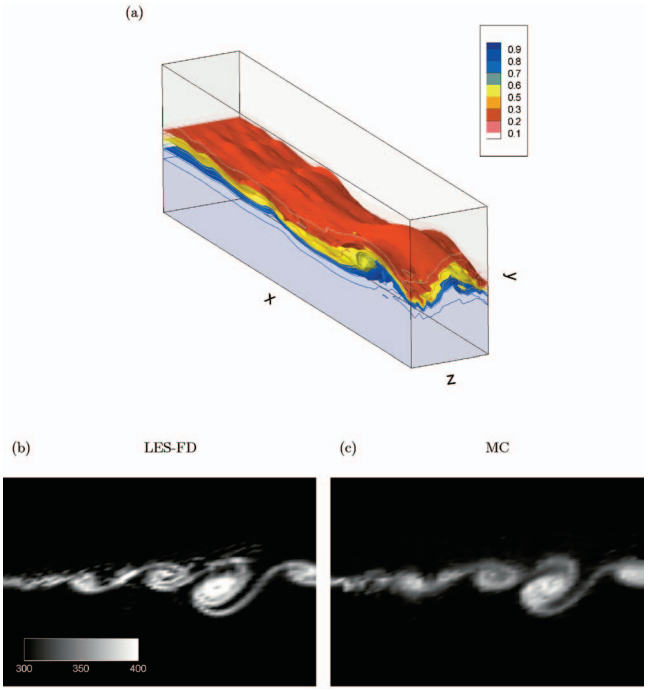

FIG. 16. (Color) Contour plots of the instantaneous filtered (a) passive scalar, and (b), (c) temperature (K) fields on a spanwise plane as obtained from LES-FD and VSFMDF, respectively, in 3D spatial mixing layer simulations.

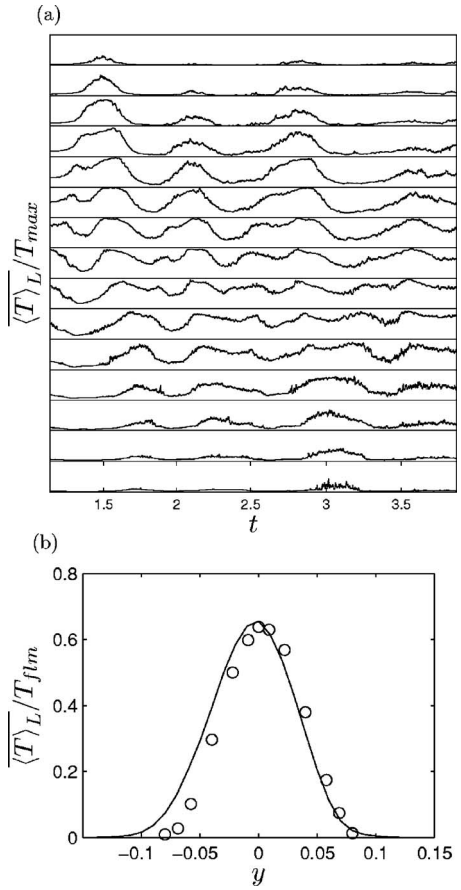

FIG. 17. (a) Time series of filtered temperature field at $x=45.7$ cm and different cross-stream locations across the shear layer, and (b) cross-stream variation of time-averaged filtered temperature field in spatial mixing layer simulations as predicted by VSFMDF. $T_{\max}$ and T_{flm} denote the maximum recorded by each probe and the adiabatic flame temperatures, respectively. The circles represent the experimental data.

The flip experiment predictions also demonstrate the same features as the laboratory observations. The time-averaged filtered temperature profiles in these predictions are integrated along the cross-stream direction to obtain the product thicknesses, as defined in the experiment,[37]

$$\delta_{P1}=\int_{-\infty}^{+\infty}\frac{C_p\overline{\langle T\rangle_L}}{c_{01}\Delta Q}dy,\quad \delta_{P2}=\int_{-\infty}^{+\infty}\frac{C_p\overline{\langle T\rangle_L}}{c_{02}\Delta Q}dy, \tag{39}$$

where C_p is the molar heat capacity of the carrier gas and ΔQ is the amount of heat release per mole of the reactant. Figure 18 shows the comparison of product thicknesses obtained from VSFMDF with the experimental data. Consistent with the experiment, the 1% thickness δ_1 is used to normalize the product thicknesses. The 1% thickness is defined as the distance at which the mean temperature rise is equal to 1% of the maximum mean temperature. In the experiment, a mean value of $\delta_1/(x-x_0)=0.165$ (where $x-x_0=45.7$ cm) is used to normalize all the product thicknesses. As shown in this figure, at low concentration ratios, the product thicknesses vary almost linearly with the concentration ratio, as the low-speed reactant reacts with an excessive amount of high-speed reactant. At high concentration ratios, the product thicknesses reach asymptotic limits. These limits correspond to the reaction of the high-speed reactant with an excessive amount of low-speed reactant. As a result, the amount of product shows little increase with the concentration ratio. As shown in this figure, the VSFMDF predictions compare reasonably well with the experimental data.

TABLE I. Computational times for the three-dimensional temporal mixing layer simulations.

Simulation	Grid resolution	Normalized CPU time per unit simulation time
Smagorinsky	33^3	1
VSFMDF	33^3	15.6
DNS	193^3	1655.2

F. Computational times

To evaluate the computational requirements of VSFMDF, the computational times are measured for simulation (i). Table I lists the CPU times corresponding to LES via the Smagorinsky[36] SGS closure, VSFMDF, and DNS. The simulations are performed on a SGI Altix 3300 computer with twelve 1.3 GHz Intel Itanium processors. In VSFMDF, 320 particles per grid point ($N_E=40$) are used. It is observed that the computational time for VSFMDF is significantly less than that for DNS. Considering the close agreement between VSFMDF and DNS results, this suggests that VSFMDF can be employed for simulations of reacting flows for which DNS is not feasible.

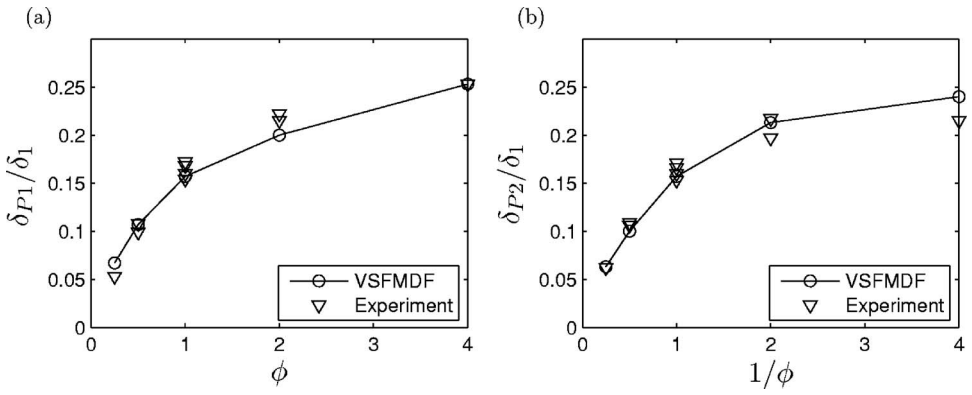

FIG. 18. Product thickness based on (a) high-speed stream, and (b) low-speed stream concentrations as obtained by VSFMDF in spatial mixing layer simulations.

VI. SUMMARY AND CONCLUDING REMARKS

The filtered density function (FDF) methodology has proven to be very effective for large eddy simulation (LES) of turbulent reactive flows. In previous investigations, the marginal FDF of the scalar, that of the velocity, and that of the joint velocity-scalar with constant-density were considered. The objective of the present work is to develop the joint velocity-scalar filtered mass density function (VSFMDF) methodology for variable-density turbulent reacting flows. For this purpose, the exact transport equation governing the evolution of the FDF is derived. It is shown that effects of SGS convection and chemical reaction appear in closed forms. The unclosed terms are modeled in a fashion similar to those typically followed in probability density function (PDF) methods in Reynolds-averaged simulations (RAS). The modeled FDF transport equation is solved numerically by a Lagrangian Monte Carlo (MC) scheme via consideration of a system of equivalent stochastic differential equations (SDEs). These SDEs are discretized via the Euler-Maruyamma discretization.

The consistency and accuracy of the VSFMDF are assessed in LES of a temporally developing mixing layer involving the transport of a passive scalar. This assessment is made by comparing the moments obtained from the MC solver with those obtained by solving the corresponding transport equations directly by the finite-difference method (LES-FD). The LES-FD equations are closed by including the moments from the MC solver. The consistency of the MC solution are demonstrated by good agreement of the first two SGS moments with those obtained by LES-FD. The VSFMDF predictions are compared with those obtained using the Smagorinsky[36] SGS closure. All of the results are also compared with direct numerical simulation (DNS) data of the same flow. It is shown that the VSFMDF performs well in predicting some of the phenomena pertaining to the SGS transport. Most of the overall flow statistics, including the mean field, the resolved and total stresses are in good agreement with DNS data. The temporal simulations are performed with several free-stream density ratios. The objective of these simulations is to evaluate the capability of the VSFMDF methodology to predict the variable density effects in turbulence. It is shown that the features pertaining to variable density shear layers, such as shift in centerline position and reduction in growth rate compare quite well with DNS data. The VSFMDF methodology is also applied to a three-dimensional spatially developing shear layer. This flow involves a fast chemical reaction with nonpremixed reactants. The predictions are appraised by comparison with laboratory data. The agreement is reasonably good and the VSFMDF predictions capture many of the features of this flow as observed in the experiment.

ACKNOWLEDGMENTS

This work is sponsored by the U.S. Air Force Office of Scientific Research under Grant No. FA9550-06-1-0015 (Program Manager: Dr. Julian M. Tishkoff), the National Science Foundation under Grant No. CTS-0426857, and the Office of the Secretary of Defense under Contract No. FA9101-04-C-0014. The computations were performed on the National Science Foundation Terascale Computing System at the Pittsburgh Supercomputing Center and at the National Center for Supercomputing Applications at the University of Illinois at Urbana.

[1] S. B. Pope, *Turbulent Flows* (Cambridge University Press, Cambridge, 2000).
[2] P. Givi, "Filtered density function for subgrid scale modeling of turbulent combustion," AIAA J. **44**, 16 (2006).
[3] S. B. Pope, "Computations of turbulent combustion: Progress and challenges," Sym. (Int.) Combust., [Proc.] **23**, 591 (1990).
[4] P. Givi, "Model free simulations of turbulent reactive flows," Prog. Energy Combust. Sci. **15**, 1 (1989).
[5] R. W. Bilger, S. B. Pope, K. N. C. Bray, and J. F. Driscoll, "Paradigms in turbulent combustion research," Proc. Combust. Inst. **30**, 21 (2005).
[6] C. K. Madnia and P. Givi, "Direct numerical simulation and large eddy simulation of reacting homogeneous turbulence," in *Large Eddy Simulations of Complex Engineering and Geophysical Flows*, edited by B. Galperin and S. A. Orszag (Cambridge University Press, Cambridge, 1993), Chap. 15, pp. 315–346.
[7] S. H. Frankel, V. Adumitroaie, C. K. Madnia, and P. Givi, "Large eddy simulations of turbulent reacting flows by assumed PDF methods," in *Engineering Applications of Large Eddy Simulations*, edited by S. A. Ragab and U. Piomelli (ASME, New York, 1993), FED-Vol. 162, pp. 81–101.
[8] F. Gao and E. E. O'Brien, "A large-eddy simulation scheme for turbulent reacting flows," Phys. Fluids A **5**, 1282 (1993).
[9] P. J. Colucci, F. A. Jaberi, P. Givi, and S. B. Pope, "Filtered density function for large eddy simulation of turbulent reacting flows," Phys. Fluids **10**, 499 (1998).
[10] F. A. Jaberi, P. J. Colucci, S. James, P. Givi, and S. B. Pope, "Filtered mass density function for large eddy simulation of turbulent reacting flows," J. Fluid Mech. **401**, 85 (1999).
[11] L. Y. M. Gicquel, P. Givi, F. A. Jaberi, and S. B. Pope, "Velocity filtered density function for large eddy simulation of turbulent flows," Phys. Fluids **14**, 1196 (2002).
[12] X. Y. Zhou and J. C. F. Pereira, "Large eddy simulation (2D) of a reacting plane mixing layer using filtered density function," Flow, Turbul. Combust. **64**, 279 (2000).
[13] S. James and F. A. Jaberi, "Large scale simulations of two-dimensional nonpremixed methane jet flames," Combust. Flame **123**, 465 (2000).
[14] V. Raman, H. Pitsch, and R. O. Fox, "Hybrid large-eddy simulation/Lagrangian filtered-density-function approach for simulating turbulent combustion," Combust. Flame **143**, 56 (2005).
[15] M. R. H. Sheikhi, T. G. Drozda, P. Givi, F. A. Jaberi, and S. B. Pope, "Large eddy simulation of a turbulent nonpremixed piloted methane jet flame (Sandia flame D)," Proc. Combust. Inst. **30**, 549 (2005).
[16] E. van Vliet, J. J. Derksen, and H. E. A. van den Akker, "Turbulent mixing in a tubular reactor: Assessment of an FDF/LES approach," AIChE J. **51**, 725 (2005).
[17] S. C. Garrick, F. A. Jaberi, and P. Givi, "Large eddy simulation of scalar transport in a turbulent jet flow," in *Recent Advances in DNS and LES*, Vol. 54 in Fluid Mechanics and its Applications, edited by D. Knight and L. Sakell (Kluwer Academic, Dordrecht, 1999), pp. 155–166.
[18] S. Heinz, "On Fokker-Planck equations for turbulent reacting flows. Part 2. Filter density function for large eddy simulation," Flow, Turbul. Combust. **70**, 153 (2003).
[19] V. Raman, H. Pitsch, and R. O. Fox, "Consistent hybrid LES-FDF formulation for the simulation of turbulent combustion," in *Annual Research Briefs, 2004* (Center for Turbulence Research, NASA Ames/Stanford University, Stanford, CA, 2004), pp. 231–241.
[20] L. Lu, Z. Ren, V. Raman, S. B. Pope, and H. Pitsch, "LES/FDF/ISAT computations of turbulent flames," in *Proceedings of the 2004 Summer Program* (Center for Turbulence Research, NASA Ames/Stanford University, Stanford, CA, 2004), pp. 283–294.

[21] M. Carrara and P. Desjardin, "A probabilistic approach to modeling separated two-phase flows for large eddy simulation," Bull. Am. Phys. Soc. **49**, 136 (2004).
[22] V. Raman, D. Cook, and H. Pitsch, "Hybrid LES/FDF simulation of a non-premixed bluff-body stabilized flame," Bull. Am. Phys. Soc. **49**, 57 (2004).
[23] T. G. Drozda, "Implementation of LES/SFMDF for prediction of nonpremixed turbulent flames," Ph.D. thesis, Department of Mechanical Engineering, University of Pittsburgh, Pittsburgh, Pennsylvania, 2005.
[24] J. Réveillon and L. Vervisch, "Subgrid-scale turbulent micromixing: Dynamic approach," AIAA J. **36**, 336 (1998).
[25] C. M. Cha and P. Troullet, "A subgrid-scale mixing model for large-eddy simulations of turbulent reacting flows using the filtered density function," Phys. Fluids **15**, 1496 (2003).
[26] C. Tong, "Measurements of conserved scalar filtered density function in a turbulent jet," Phys. Fluids **13**, 2923 (2001).
[27] D. Wang and C. Tong, "Conditionally filtered scalar dissipation, scalar diffusion, and velocity in a turbulent jet," Phys. Fluids **14**, 2170 (2002).
[28] A. G. Rajagopalan and C. Tong, "Experimental investigation of scalar-scalar-dissipation filtered joint density function and its transport equation," Phys. Fluids **15**, 227 (2003).
[29] D. Wang, C. Tong, and S. B. Pope, "Experimental study of velocity filtered joint density function for large eddy simulation," Phys. Fluids **16**, 3599 (2004).
[30] D. Wang and C. Tong, "Experimental study of velocity-scalar filtered joint density function for LES of turbulent combustion," Proc. Combust. Inst. **30**, 567 (2005).
[31] A. Chandy, G. M. Goldin, and S. H. Frankel, "Modeling turbulent non-premixed jet flames using Fluent's PDF transport model: Effect of mixing model on flame extinction," in *30th International Symposium on Combustion, Abstracts of Work-In-Progress Posters* (The Combustion Institute, Pittsburgh, 2004), p. 447.
[32] D. J. Glaze, S. H. Frankel, and J. C. Hewson, "Non-premixed turbulent jet mixing using LES with the FMDF model," in *30th International Symposium on Combustion, Abstracts of Work-In-Progress Posters* (The Combustion Institute, Pittsburgh, 2004), p. 79.
[33] R. O. Fox, *Computational Models for Turbulent Reacting Flows* (Cambridge University Press, Cambridge, 2003).
[34] S. Heinz, *Statistical Mechanics of Turbulent Flows* (Springer, New York, 2003).
[35] C. K. Madnia, F. A. Jaberi, and P. Givi, "Large eddy simulation of heat and mass transport in turbulent flows," in *Handbook of Numerical Heat Transfer*, 2nd ed., edited by W. J. Minkowycz, E. M. Sparrow, and J. Y. Murthy (Wiley, New York, 2006), Chap. 5, pp. 167–189.
[36] J. Smagorinsky, "General circulation experiments with the primitive equations. I. The basic experiment," Mon. Weather Rev. **91**, 99 (1963).
[37] M. G. Mungal and P. E. Dimotakis, "Mixing and combustion with low heat release in a turbulent mixing layer," J. Fluid Mech. **148**, 349 (1984).
[38] G. L. Brown and A. Roshko, "On density effects and large structure in turbulent mixing layers," J. Fluid Mech. **64**, 775 (1974).
[39] C. Pantano and S. Sarkar, "A study of compressibility effects in the high-speed turbulent shear layer using direct simulation," J. Fluid Mech. **451**, 329 (2002).
[40] P. Chassaing, R. A. Antonia, F. Anselmet, L. Joly, and S. Sarkar, *Variable Density Fluid Turbulence* (Kluwer Academic, Dordrecht, 2002).
[41] W. T. Ashurst and A. R. Kerstein, "One-dimensional turbulence: Variable-density formulation and application to mixing layers," Phys. Fluids **17**, 025107 (2005).
[42] S. K. Lele, "Compressibility effects on turbulence," Annu. Rev. Fluid Mech. **26**, 211 (1994).
[43] P. A. Libby and F. A. Williams, *Turbulent Reacting Flows*, Vol. 44 of Topics in Applied Physics (Springer, Heidelberg, 1980).
[44] S. B. Pope, "PDF methods for turbulent reactive flows," Prog. Energy Combust. Sci. **11**, 119 (1985).
[45] R. W. Bilger, "Molecular transport effects in turbulent diffusion flames at moderate Reynolds number," AIAA J. **20**, 962 (1982).
[46] U. Piomelli, "Large-eddy simulation: Achievements and challenges," Prog. Aerosp. Sci. **35**, 335 (1999).
[47] C. Meneveau and J. Katz, "Scale-invariance and turbulence models for large-eddy simulations," Annu. Rev. Fluid Mech. **32**, 1 (2000).
[48] B. J. Geurts, *Modern Simulation Strategies for Turbulent Flow* (R. T. Edwards, Philadelphia, 2001).
[49] P. Sagaut, *Large Eddy Simulation for Incompressible Flows* (Springer, New York, 2001).
[50] E. E. O'Brien, in Ref. 43, Chap. 5, pp. 185–218.
[51] B. Vreman, B. Geurts, and H. Kuerten, "Realizability conditions for the turbulent stress tensor in large-eddy simulation," J. Fluid Mech. **278**, 351 (1994).
[52] S. Karlin and H. M. Taylor, *A Second Course in Stochastic Processes* (Academic, New York, 1981).
[53] N. Wax, *Selected Papers on Noise and Stochastic Processes* (Dover, New York, 1954).
[54] C. W. Gardiner, *Handbook of Stochastic Methods* (Springer, New York, 1990).
[55] D. C. Haworth and S. B. Pope, "A generalized Langevin model for turbulent flows," Phys. Fluids **29**, 387 (1986).
[56] T. D. Dreeben and S. B. Pope, "Probability density function and Reynolds-stress modeling of near-wall turbulent flows," Phys. Fluids **9**, 154 (1997).
[57] M. R. H. Sheikhi, T. G. Drozda, P. Givi, and S. B. Pope, "Velocity-scalar filtered density function for large eddy simulation of turbulent flows," Phys. Fluids **15**, 2321 (2003).
[58] H. Risken, *The Fokker-Planck Equation, Methods of Solution and Applications* (Springer, New York, 1989).
[59] M. Muradoglu, P. Jenny, S. B. Pope, and D. A. Caughey, "A consistent hybrid-volume/particle method for the PDF equations of turbulent reactive flows," J. Comput. Phys. **154**, 342 (1999).
[60] M. Muradoglu, S. B. Pope, and D. A. Caughey, "The hybrid method for the PDF equations of turbulent reactive flows: Consistency conditions and correction algorithms," J. Comput. Phys. **172**, 841 (2001).
[61] P. E. Kloeden, E. Platen, and H. Schurz, *Numerical Solution of Stochastic Differential Equations Through Computer Experiments*, corrected second printing edition (Springer, New York, 1997).
[62] I. I. Gikhman and A. V. Skorokhod, *Stochastic Differential Equations* (Springer, New York, 1972).
[63] M. H. Carpenter, "A high-order compact numerical algorithm for supersonic flows," in *Twelfth International Conference on Numerical Methods in Fluid Dynamics*, Vol. 371 of Lecture Notes in Physics, edited by K. W. Morton (Springer, New York, 1990), pp. 254–258.
[64] C. A. Kennedy and M. H. Carpenter, "Several new numerical methods for compressible shear-layer simulations," Appl. Numer. Math. **14**, 397 (1994).
[65] J. J. Riley and R. W. Metcalfe, "Direct numerical simulations of a perturbed, turbulent mixing layer," AIAA Paper 80-0274, 1980.
[66] N. D. Sandham and W. C. Reynolds, "Three-dimensional simulations of large eddies in the compressible mixing layer," J. Fluid Mech. **224**, 133 (1991).
[67] R. D. Moser and M. M. Rogers, "The three-dimensional evolution of a plane mixing layer: Pairing and transition to turbulence," J. Fluid Mech. **247**, 275 (1993).
[68] B. Vreman, B. Geurts, and H. Kuerten, "Large-eddy simulation of the turbulent mixing layer," J. Fluid Mech. **339**, 357 (1997).
[69] R. W. Metcalfe, S. A. Orszag, M. E. Brachet, S. Menon, and J. J. Riley, "Secondary instabilities of a temporally growing mixing layer," J. Fluid Mech. **184**, 207 (1987).
[70] S. J. Lin and G. M. Corcos, "The mixing layer: Deterministic models of a turbulent flow. Part 3. The effect of plane strain on the dynamics of streamwise vortices," J. Fluid Mech. **141**, 139 (1984).
[71] R. D. Moser and M. M. Rogers, "The three-dimensional evolution of a plane mixing layer: The Kelvin-Helmholtz rollup," J. Fluid Mech. **243**, 183 (1992).
[72] R. D. Moser and M. M. Rogers, "Spanwise scale selection in plane mixing layers," J. Fluid Mech. **247**, 321 (1993).
[73] N. D. Sandham and W. C. Reynolds, "Some inlet-plane effects on the numerically simulated spatially-developing mixing layer," in *Turbulent Shear Flows 6* (Springer, New York, 1989), pp. 441–454.
[74] G. Erlebacher, M. Y. Hussaini, C. G. Speziale, and T. A. Zang, "Toward the large eddy simulation of compressible turbulent flows," J. Fluid Mech. **238**, 155 (1992).
[75] T. J. Poinsot and S. K. Lele, "Boundary conditions for direct simulations of compressible viscous flows," J. Comput. Phys. **101**, 104 (1992).
[76] D. H. Rudy and J. C. Strikwerda, "Boundary conditions for subsonic compressible Navier-Stokes calculations," J. Comput. Phys. **36**, 327 (1980).
[77] S. B. Pope, "On the relation between stochastic Lagrangian models of turbulence and second-moment closures," Phys. Fluids **6**, 973 (1994).
[78] R. S. Rogallo and P. Moin, "Numerical simulation of turbulent flow," Annu. Rev. Fluid Mech. **16**, 99 (1984).

[79]A. Yoshizawa, "Statistical theory for compressible turbulent shear flows, with the application to subgrid modeling," Phys. Fluids **29**, 2152 (1986).
[80]P. Moin, W. Squires, W. H. Cabot, and S. Lee, "A dynamic subgrid-scale model for compressible turbulence and scalar transport," Phys. Fluids A **3**, 2746 (1991).
[81]A. W. Vreman, N. D. Sandham, and K. H. Luo, "Compressible mixing layer growth rate and turbulence characteristics," J. Fluid Mech. **320**, 235 (1996).
[82]R. W. Bilger, "Future progress in turbulent combustion research," Prog. Energy Combust. Sci. **26**, 367 (2000).
[83]N. Peters, *Turbulent Combustion* (Cambridge University Press, Cambridge, 2000).